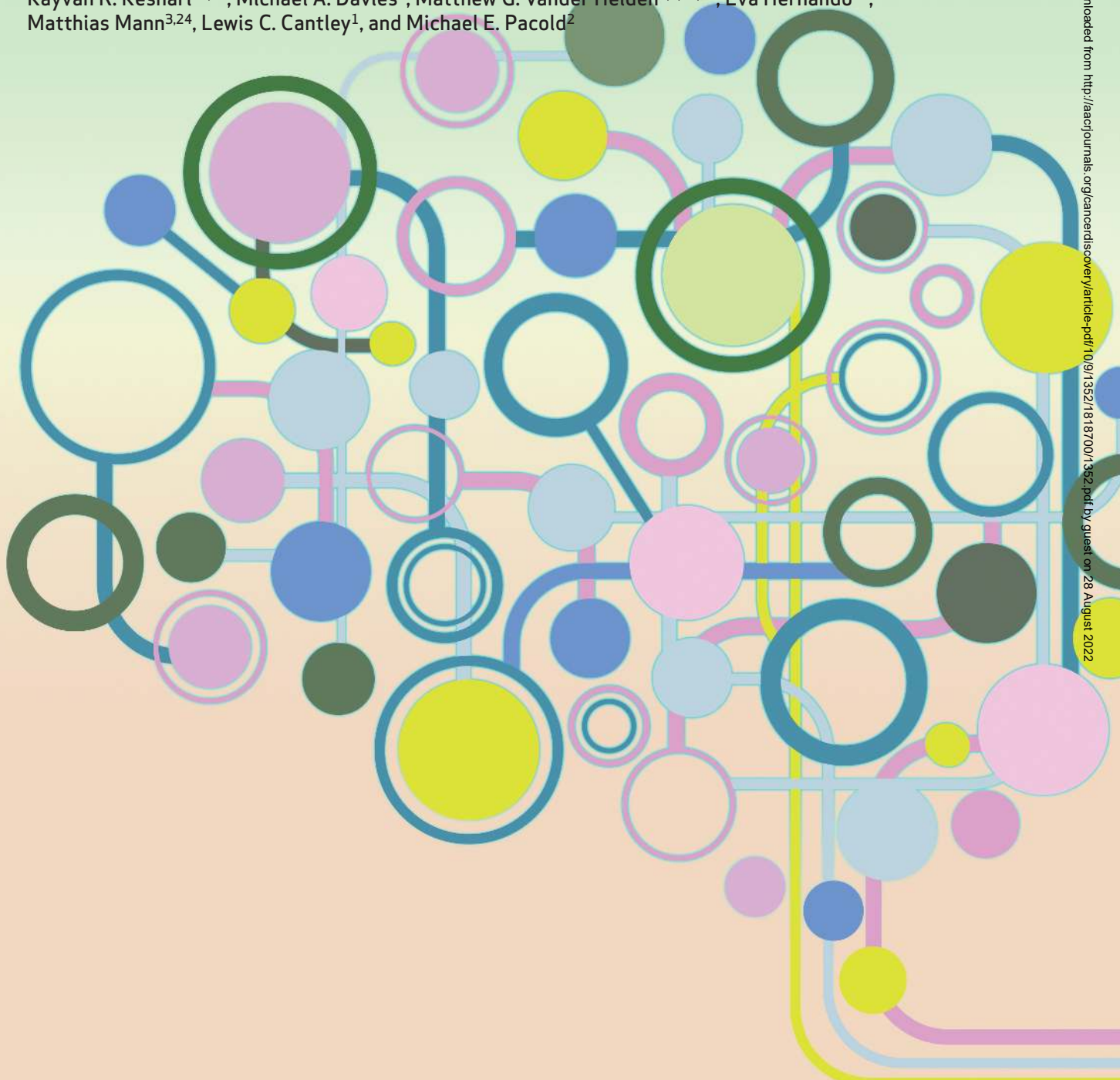


# Limited Environmental Serine and Glycine Confer Brain Metastasis Sensitivity to PHGDH Inhibition



Bryan Ngo<sup>1</sup>, Eugenie Kim<sup>2</sup>, Victoria Osorio-Vasquez<sup>2</sup>, Sophia Doll<sup>3</sup>, Sophia Bustra<sup>2</sup>, Roger J. Liang<sup>1</sup>, Alba Luengo<sup>4,5</sup>, Shawn M. Davidson<sup>6</sup>, Ahmed Ali<sup>4,5</sup>, Gino B. Ferraro<sup>7,8</sup>, Grant M. Fischer<sup>9</sup>, Roozbeh Eskandari<sup>10</sup>, Diane S. Kang<sup>11</sup>, Jing Ni<sup>12,13</sup>, Ariana Plasger<sup>1</sup>, Vinagolu K. Rajasekhar<sup>14</sup>, Edward R. Kasthuber<sup>1</sup>, Sarah Bacha<sup>1</sup>, Roshan K. Sriram<sup>1</sup>, Benjamin D. Stein<sup>1</sup>, Samuel F. Bakhom<sup>15,16</sup>, Matija Snuderl<sup>17</sup>, Paolo Cotzia<sup>17</sup>, John H. Healey<sup>14</sup>, Nello Mainolfi<sup>18</sup>, Vipin Suri<sup>18</sup>, Adam Friedman<sup>18</sup>, Mark Manfredi<sup>18</sup>, David M. Sabatini<sup>19,20,21</sup>, Drew R. Jones<sup>2,22</sup>, Min Yu<sup>11</sup>, Jean J. Zhao<sup>12,13,21</sup>, Rakesh K. Jain<sup>7,8</sup>, Kayvan R. Keshari<sup>10,23</sup>, Michael A. Davies<sup>9</sup>, Matthew G. Vander Heiden<sup>4,5,12,21</sup>, Eva Hernando<sup>17</sup>, Matthias Mann<sup>3,24</sup>, Lewis C. Cantley<sup>1</sup>, and Michael E. Pacold<sup>2</sup>



## ABSTRACT

A hallmark of metastasis is the adaptation of tumor cells to new environments. Metabolic constraints imposed by the serine and glycine-limited brain environment restrict metastatic tumor growth. How brain metastases overcome these growth-prohibitive conditions is poorly understood. Here, we demonstrate that 3-phosphoglycerate dehydrogenase (PHGDH), which catalyzes the rate-limiting step of glucose-derived serine synthesis, is a major determinant of brain metastasis in multiple human cancer types and preclinical models. Enhanced serine synthesis proved important for nucleotide production and cell proliferation in highly aggressive brain metastatic cells. *In vivo*, genetic suppression and pharmacologic inhibition of PHGDH attenuated brain metastasis, but not extracranial tumor growth, and improved overall survival in mice. These results reveal that extracellular amino acid availability determines serine synthesis pathway dependence, and suggest that PHGDH inhibitors may be useful in the treatment of brain metastasis.

**SIGNIFICANCE:** Using proteomics, metabolomics, and multiple brain metastasis models, we demonstrate that the nutrient-limited environment of the brain potentiates brain metastasis susceptibility to serine synthesis inhibition. These findings underscore the importance of studying cancer metabolism in physiologically relevant contexts, and provide a rationale for using PHGDH inhibitors to treat brain metastasis.

## INTRODUCTION

Metastasis is the end result of an evolutionary process in which tumor cells adapt to different tissue environments (1, 2). Despite efforts to identify novel oncogenic mutations that drive distant metastasis, whole-genome sequencing studies have revealed striking similarities in the array of driver gene mutations between primary tumors and paired metastases (3, 4). These findings raise the possibility that cancer cell-specific metabolic adaptation, imposed by the selective pressure of the metastatic niche, enables tumor cells to colonize distant organs. Targeting the metabolic vulnerabilities of metastasis may offer effective treatments for cancers that have spread to distant organs such as the brain.

Brain metastasis (BrM) is the most common intracranial malignancy in adults and is often fatal (5–8). Growing

evidence indicates that brain metastases possess unique metabolic characteristics compared with metastases to other sites (9–12). Multiple studies have shown that the establishment and growth of brain metastases depends on cooperative cellular interactions between tumor cells and specialized cells within the central nervous system (CNS), including astrocytes, microglia, neurons, and endothelial cells (5, 9–11, 13–18). Surprisingly, very little is known about how cancer cells adapt metabolically to the microenvironment of the brain, which is low in growth factors, metabolic intermediates, and proteins relative to the plasma (19–21). Both the brain interstitial fluid (ISF) and cerebrospinal fluid (CSF), which buffers and bathes the brain and spinal cord, are severely depleted of amino acids relative to plasma (20, 22, 23). It is unknown if the amino acid-depleted environment

<sup>1</sup>Sandra and Edward Meyer Cancer Center, Weill Cornell Medicine, New York, New York. <sup>2</sup>Department of Radiation Oncology, Perlmutter Cancer Center and NYU Langone Health, New York, New York. <sup>3</sup>Department of Proteomics and Signal Transduction, Max Planck Institute of Biochemistry, Martinsried, Germany. <sup>4</sup>Koch Institute for Integrative Cancer Research, Cambridge, Massachusetts. <sup>5</sup>Department of Biology, Massachusetts Institute of Technology, Cambridge, Massachusetts. <sup>6</sup>Lewis-Sigler Institute for Integrative Genomics, Princeton University, Princeton, New Jersey. <sup>7</sup>Edwin L. Steele Laboratories, Department of Radiation Oncology, Massachusetts General Hospital, Boston, Massachusetts. <sup>8</sup>Harvard Medical School, Boston, Massachusetts. <sup>9</sup>Departments of Translational Molecular Pathology, Melanoma Medical Oncology, Systems Biology, The University of Texas MD Anderson Cancer Center, Houston, Texas. <sup>10</sup>Department of Radiology, Memorial Sloan Kettering Cancer Center, New York, New York. <sup>11</sup>Department of Stem Cell Biology and Regenerative Medicine, University of Southern California Norris Comprehensive Cancer Center, Keck School of Medicine, Los Angeles, California. <sup>12</sup>Department of Cancer Biology, Dana-Farber Cancer Institute, Boston, Massachusetts. <sup>13</sup>Department of Biological Chemistry and Molecular Pharmacology, Harvard Medical School, Boston, Massachusetts. <sup>14</sup>Department of Surgery, Memorial Sloan Kettering Cancer Center, New York, New York. <sup>15</sup>Human Oncology and Pathogenesis Program, Memorial Sloan Kettering Cancer Center, New York, New York. <sup>16</sup>Department of Radiation Oncology, Memorial Sloan Kettering Cancer Center, New York, New York. <sup>17</sup>Department of Pathology,

New York University Langone Health, New York, New York. <sup>18</sup>Raze Therapeutics, Cambridge, Massachusetts. <sup>19</sup>Whitehead Institute for Biomedical Research, Cambridge, Massachusetts. <sup>20</sup>Howard Hughes Medical Institute, Department of Biology, Massachusetts Institute of Technology, Cambridge, Massachusetts. <sup>21</sup>Broad Institute, Cambridge, Massachusetts. <sup>22</sup>Metabolomics Core Resource Laboratory, NYU Langone Health, New York, New York. <sup>23</sup>Molecular Pharmacology Program, Memorial Sloan Kettering Cancer Center, New York, New York. <sup>24</sup>Faculty of Health and Medical Sciences, NNF Center for Protein Research, University of Copenhagen, Copenhagen, Denmark.

**Note:** Supplementary data for this article are available at Cancer Discovery Online (<http://cancerdiscovery.aacrjournals.org/>).

B. Ngo, E. Kim, and V. Osorio-Vasquez contributed equally to this article.

**Corresponding Authors:** Michael E. Pacold, NYU Langone Health, 522 1st Avenue, Smilow 907G, New York, NY 10016. Phone: 212-263-9181; E-mail: michael.pacold@nyulangone.org; and Lewis C. Cantley, Weill Cornell Medicine, Belfer Research Building, 413 E. 69th Street, New York, NY 10021. Phone: 646-962-6297; E-mail: lcantley@med.cornell.edu

Cancer Discov 2020;10:1352–73

doi: 10.1158/2159-8290.CD-19-1228

©2020 American Association for Cancer Research.

of the ISF or CSF selects for targetable metabolic dependencies in brain metastases.

Amino acids are important for the biosynthesis of proteins, nucleotides, lipids, antioxidants, and tricarboxylic acid (TCA) cycle intermediates, all of which are needed for cell growth. When exogenous amino acids are limiting, cells can synthesize nonessential amino acids (NEAA) *de novo*, including serine, glycine, and aspartate (24–35). Diversion of glycolytic intermediates into the serine and glycine biosynthesis pathway is commonly observed in melanoma and triple-negative breast cancer (TNBC; ER<sup>-</sup>/PR<sup>-</sup>/HER2<sup>-</sup>; refs. 36, 37). This specific metabolic alteration is driven by the increased expression of 3-phosphoglycerate dehydrogenase (PHGDH) through focal genomic amplifications, transcriptional changes, or post-translational regulation (36–39). Attempts to therapeutically target PHGDH with small molecules have largely yielded modest results *in vivo* (40–43). Therefore, we postulated that the phenotypic penetrance of PHGDH inhibitors may depend on local extracellular serine and glycine concentrations within the tumor microenvironment.

Here we investigate the mechanisms contributing to metastatic cancer cell survival within the brain microenvironment. We demonstrate that limited microenvironmental serine and glycine enforce brain metastasis dependency on *de novo* serine synthesis. Genetic suppression and pharmacologic inhibition of PHGDH suppressed brain metastasis *in vivo*, but not extracranial tumor growth. These results indicate that the limited nutrient environment of the brain selects for cancer cells with distinct metabolic dependencies, and suggest that improved PHGDH inhibitors could be clinically useful in treating patients with brain metastasis.

## RESULTS

### PHGDH and Glucose-Derived Serine Are Enriched in Aggressive TNBC Brain Metastatic Cells

To gain insight into the molecular events underlying brain metastasis, we analyzed both the proteomes and labeled metabolomes of parental, aggressive, and indolent TNBC BrM cells (44–47). To generate BrM clones that differ in their ability to colonize the brain, we performed *in vivo* selection using the MDA-MB-231 TNBC cell line (Fig. 1A; refs. 5, 11, 13, 14, 18). Aggressive TNBC BrM cells generated multifocal lesions in the cerebrum, cerebellum, and brain stem of mice, whereas indolent TNBC BrM cells failed to form detectable brain metastases at approximately 10 weeks (2.5 months; Fig. 1B and C; Supplementary Fig. S1A).

Comparative proteomic expression profiling of aggressive and indolent TNBC BrM cells using an optimized, high-sensitivity, label-free protein expression profiling workflow quantified approximately 7,000 proteins per sample with excellent reproducibility (Supplementary Fig. S1B–S1D; refs. 45–48). Our analysis yielded protein expression profiles of the parental, indolent, and aggressive TNBC BrM cells that segregated independently by principal component analysis (PCA), indicating that each population is phenotypically distinct (Fig. 1D). PHGDH, the first enzyme in the glucose-derived serine biosynthesis pathway, was the most significantly upregulated protein in aggressive TNBC BrM

cells compared to indolent TNBC BrM cells (FDR < 0.01; Fig. 1E–G).

PHGDH catalyzes the first and rate-limiting step in the canonical, glucose-derived serine synthesis pathway, and uses NAD<sup>+</sup> as a cofactor to oxidize the glycolytic intermediate 3-phosphoglycerate (3PG) to 3-phosphohydroxypyruvate (3-PHP; Fig. 1H). Subsequent enzymes in the serine synthesis pathway convert 3-PHP into serine via transamination [phosphoserine aminotransferase 1 (PSAT1)] and phosphate ester hydrolysis [phosphoserine phosphatase (PSPH)]. Serine is essential for synthesis of proteins and other biomolecules needed for cell proliferation, including glycine, cysteine, nucleotides, phosphatidylserine, sphingosine, and charged folates required for one-carbon metabolism (49).

To understand the metabolic consequences of increased PHGDH expression in brain metastasis, we cultured aggressive and indolent TNBC BrM cells with uniformly carbon-labeled <sup>13</sup>C glucose (U-<sup>13</sup>C-glucose) and measured the mole percent enrichment of glucose-derived metabolites by gas chromatography-mass spectrometry (GC-MS). Interestingly, glucose-derived serine and glycine exhibited the greatest increase in glucose-derived <sup>13</sup>C incorporation in aggressive TNBC BrM cells compared with indolent TNBC BrM cells (Fig. 1I). This observation supports the hypothesis that glucose-derived serine and glycine synthesis is significantly upregulated in aggressive TNBC BrM cells relative to indolent TNBC BrM cells.

### Brain Metastases from Different Tumor Types Upregulate Serine Synthesis

To determine whether enhanced serine synthesis is a general feature of brain metastasis, we sought to validate our findings in complementary models of breast cancer and melanoma brain metastasis. Approximately one quarter of human breast cancers have amplifications in the *HER2* (*ERBB2*) proto-oncogene, and up to 50% of patients with HER2-positive breast cancer are at risk of developing brain metastasis (50). To test whether direct implantation of a HER2-positive breast cancer cell line, BT474, intracranially (ICr) in the brain parenchyma resulted in a functional increase in serine synthesis relative to tumors in the mammary fat pad (MFP) *in vivo*, we infused tumor-bearing mice with <sup>13</sup>C glucose and examined serine labeling in tumor tissue. BT474 brain metastatic tumors exhibited a 2-fold increase in serine labeling from glucose compared with the MFP tumors, consistent with the finding that PHGDH expression was increased in intracranial tumor cells compared with cells implanted into the MFP (Fig. 2A; Supplementary Fig. S2A and S2B). In addition, isolated patient-derived, estrogen-positive (ER<sup>+</sup>) circulating tumor cells (CTC) that exhibited tropism toward the brain (BrM3) had a dramatic increase in PHGDH expression compared with first-generation parental clones (BrX50 Parental; Supplementary Fig. S2C and S2D).

Next, we analyzed and compared transcriptomic data collected from three melanoma cell lines (A375, WM1361A, and MeWo) implanted subcutaneously and intracranially. Transcript levels for PHGDH and PSAT1 were increased in intracranial tumors relative to subcutaneous tumors (Fig. 2B). Furthermore, gene ontology (GO) analysis revealed that the serine biosynthesis gene set was significantly enriched in

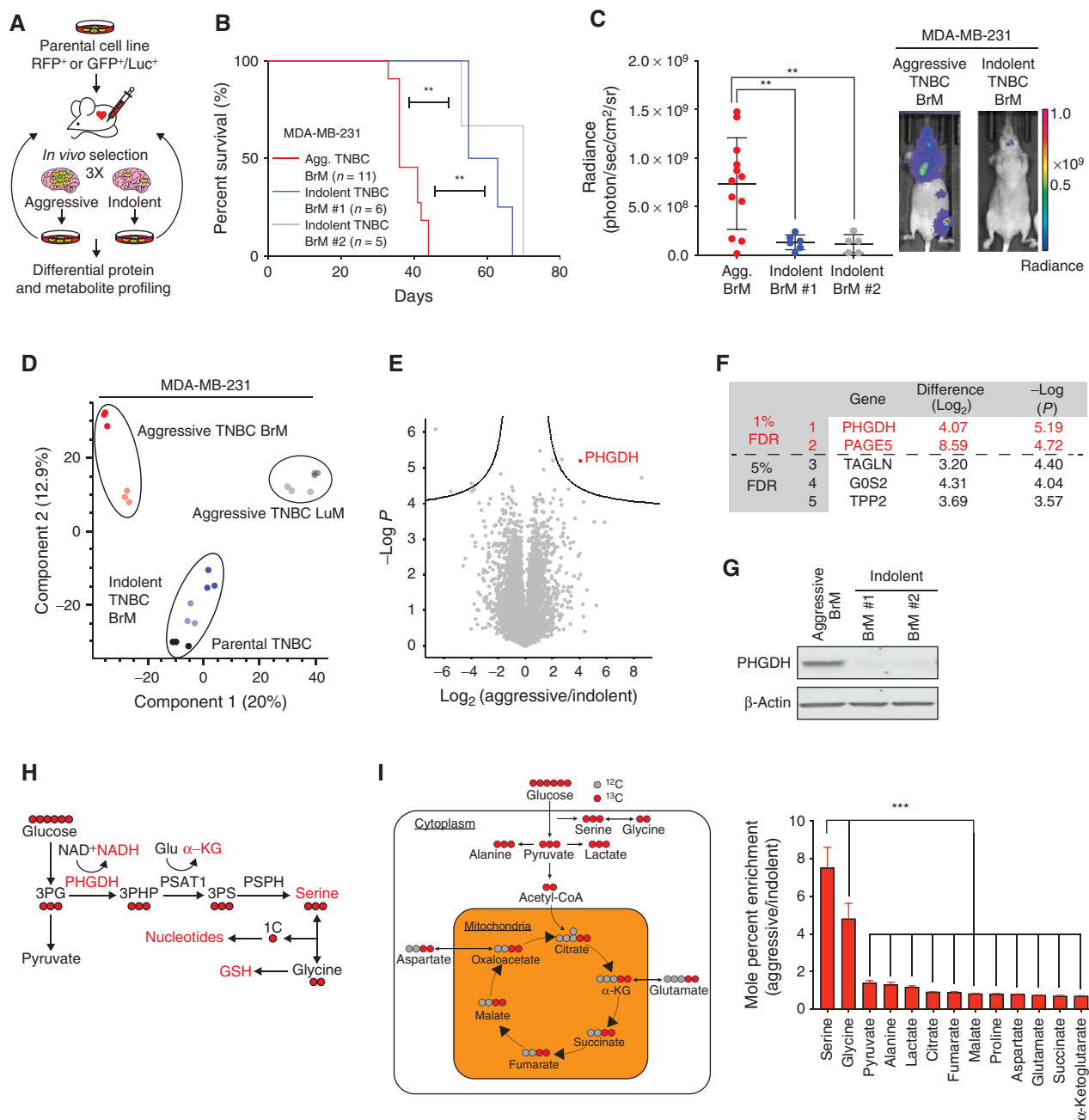


**Figure 1.** Generation and characterization of aggressive and indolent brain metastatic cells. **A**, Schematic of the generation and characterization of TNBC BrM cells. **B**, Kaplan-Meier plot showing disease-specific survival of mice injected with aggressive TNBC (black) or indolent (blue and gray) BrM cells. Significance was tested using the log-rank test. **C**, Radiance (photons/second/cm<sup>2</sup>/sr) as measured by BLI of aggressive and indolent TNBC BrM cells four weeks after intracardiac injection. **D**, PCA plot of proteome derived from two aggressive brain metastatic clones (shades of red), two aggressive lung metastatic clones (shades of gray), two indolent brain metastatic clones (shades of blue), and parental MDA-MB-231 TNBC cells (black). **E**, Volcano plot of the *P* value versus the log<sub>2</sub> protein abundance differences between aggressive and indolent TNBC BrM cells. Solid lines indicate FDR < 0.01. **F**, List of the five most significant differentially expressed proteins between aggressive and indolent TNBC BrM cells. **G**, Immunoblot of PHGDH expression in aggressive and indolent TNBC BrM cells. **H**, Schematic of the glucose-derived serine biosynthesis pathway. 3PG, 3-phosphoglycerate; 3PHP, 3-phosphohydroxypyruvate; 3PS, 3-phospho-serine; 1C, one-carbon unit; GSH, reduced glutathione; PHGDH, phosphoglycerate dehydrogenase; PSAT, phospho-serine aminotransferase; PSPH, phosphoserine phosphatase. Glucose-derived carbon atoms are indicated in red. **I**, Mole percent enrichment of metabolite labeling by U-<sup>13</sup>C-glucose in aggressive versus indolent TNBC BrM cells. For this and all subsequent figures, \* *P* < 0.05; \*\* *P* < 0.005; \*\*\* *P* < 0.0005. Significance is measured with the Mann-Whitney *U* test unless otherwise indicated. Error bars represent standard deviation unless otherwise indicated.

Downloaded from <http://aacrjournals.org/cancerdiscovery/article-pdf/10/9/1352/1818700/1352.pdf> by guest on 28 August 2022

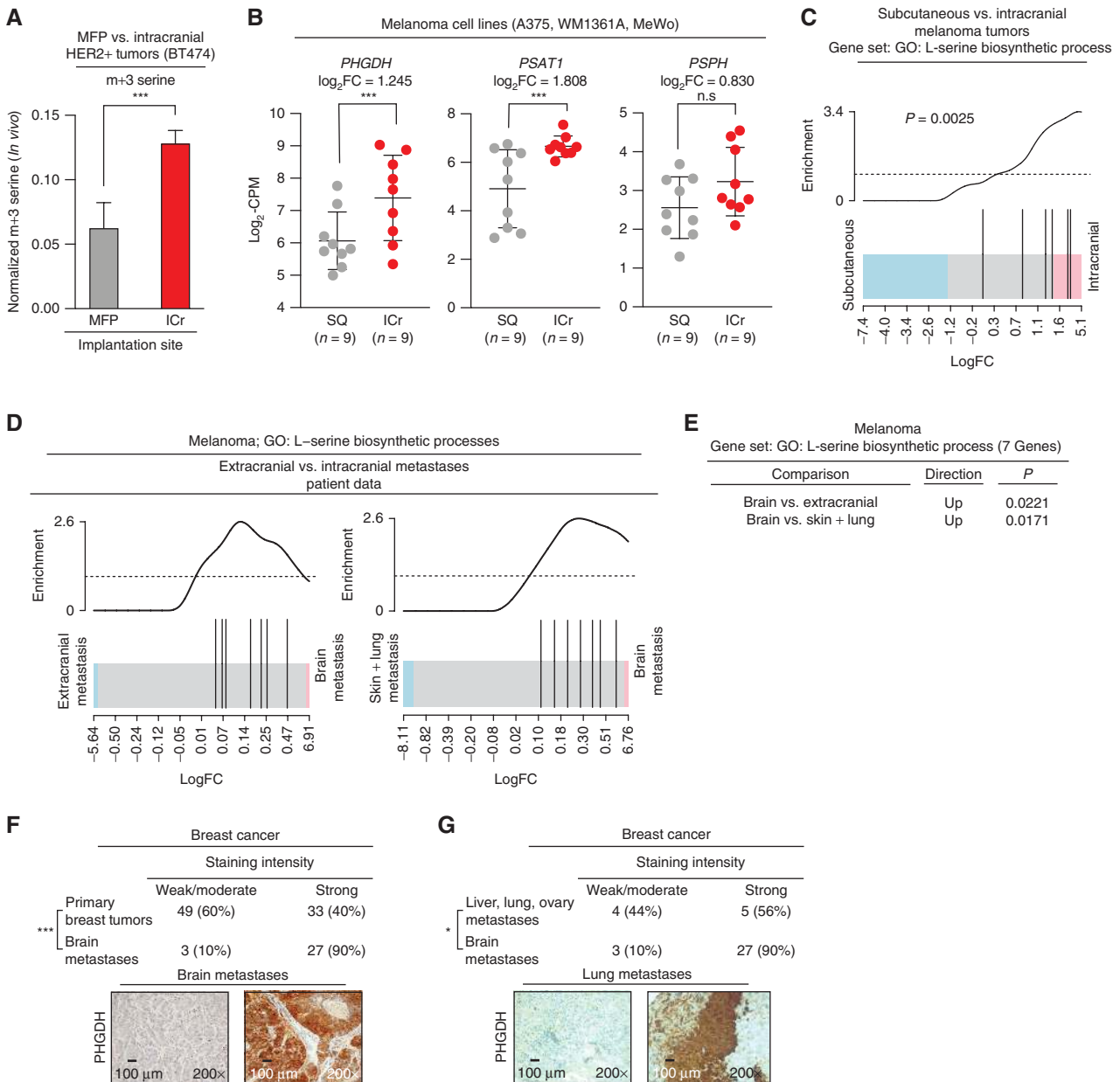


**Figure 2.** Preclinical models recapitulate enrichment of serine synthesis genes observed in human brain metastases. **A**, *In vivo* serine (m+3) labeling from U-<sup>13</sup>C-glucose in tumors derived from BT474 HER2+ breast cancer cells implanted into the MFP or ICr. **B**, RNA-sequencing expression of serine synthesis pathway genes, *PHGDH*, *PSAT1*, and *PSPH*, in implanted melanoma ICr tumors and subcutaneous (SQ) tumors derived from A375, WM1361A, and MeWo melanoma cell lines. **C**, L-serine biosynthesis gene ontology (GO) analysis of RNA-sequencing data in ICr melanoma brain metastases relative to SQ tumors in mice. **D**, L-serine GO analysis of RNA-sequencing data from melanoma brain metastases and extracranial metastases in patients. **E**, *P* values for **D** showing enrichment of L-serine biosynthesis genes in brain metastases relative to extracranial metastases (lung, liver, bone, and intestine). **F**, IHC analysis of *PHGDH* expression in human breast cancer brain metastases and primary breast tumors. Significance was determined using Fisher exact test. *P* value = 0.0001. Scale bar, 100 μm. **G**, IHC analysis of *PHGDH* expression in human breast cancer brain metastases and extracranial metastases. Significance was determined using Fisher exact test. *P* = 0.037. Scale bar, 100 μm.

intracranial tumors relative to subcutaneously implanted tumors (Fig. 2C). These experimental results indicate that increased *PHGDH* expression and serine synthesis are characteristic of breast cancer and melanoma brain metastasis, and suggest that glucose-derived serine synthesis may be a general feature of human brain metastasis.

### Human Brain Metastases Display Enhanced Expression of Serine Synthesis Genes

Breast cancer and melanoma are the second and third most common causes of brain metastases. To address the clinical relevance of our experimental findings, we analyzed two independent clinical cohorts of brain metastases and TCGA breast

Downloaded from <http://aacrjournals.org/cancerdiscovery/article-pdf/10/9/1352/1818700/1352.pdf> by guest on 28 August 2022

cancer RNA expression data. First, GO transcriptomic analysis revealed that the serine biosynthesis gene set is enriched in melanoma brain metastases relative to both extracranial metastases (lung, bone, liver, and intestine) and primary tumors (Fig. 2D and E). Next, IHC staining for PHGDH expression in a cohort of patients with breast cancer brain metastasis showed that 90% (27 of 30) of breast cancer brain metastases had elevated PHGDH expression (Fig. 2F). This was a significantly higher percentage than the approximately 40% (33 of 82) of primary breast tumors with high PHGDH expression as reanalyzed from a previously published cohort (36). Notably, PHGDH expression was also significantly higher in breast cancer brain metastases than breast cancer extracranial metastases (lung, liver, and ovary; Fig. 2G). Finally, analysis of OncoPrint data indicated that *PHGDH* expression is 4-fold higher in TNBC tumors ( $n = 46$ ) than other breast cancer subtypes ( $n = 250$ ; from TCGA breast invasive carcinoma), and that *PHGDH* expression in breast cancer with metastatic events at 3 years ( $n = 140$ ) is 2-fold higher than breast cancer without metastatic events at 3 years ( $n = 48$ ; Supplementary Fig. S2E and S2F; ref. 14). These clinical data indicate that PHGDH expression is enriched in breast cancer and melanoma brain metastases relative to primary tumors and extracranial metastases.

### The Brain Is a Serine- and Glycine-Limited Environment

Cancer cells that colonize the brain encounter an environment deprived of exogenous serine and glycine. With the exception of glutamine, both serine and glycine are among the least abundant amino acids in the brain ISF and the CSF relative to the plasma (Supplementary Fig. S3A; refs. 20, 23). In agreement with previous studies, the concentrations of serine and glycine in mouse CSF are approximately 28  $\mu\text{mol/L}$  and approximately 5  $\mu\text{mol/L}$ , respectively, and are about 4- and 50-fold lower than the concentrations of these amino acids in mouse plasma (~100 and ~250  $\mu\text{mol/L}$ , respectively; Supplementary Fig. S3B; refs. 20, 23).

### PHGDH Is Required for Cell Proliferation in Serine- and Glycine-Limited Environments

To understand the consequences of limited microenvironmental serine and glycine on brain metastasis metabolism and proliferation, we developed cell culture media with serine and glycine concentrations comparable to plasma and cerebrospinal fluid (plasma, CSF, and -Ser/-Gly media; Supplementary Fig. S3C). We then measured the incorporation of  $^{13}\text{C}$  glucose into serine and glycine in aggressive and indolent TNBC BrM cells. PHGDH-expressing aggressive BrM cells derived 5% of their serine from glucose when cultured with plasma media. This increased to approximately 20% and approximately 25% in CSF and -Ser/-Gly media, respectively. In contrast, indolent BrM cells derived no more than approximately 15% of their serine from glucose regardless of the extracellular serine and glycine concentrations (Fig. 3A; Supplementary Fig. S3D and S3E).

Serine is essential for the production of one-carbon units needed for cell proliferation and can be taken up from the extracellular microenvironment or synthesized from glucose. We reasoned that aggressive and indolent TNBC BrM cells should proliferate at comparable rates in plasma media where extracel-

lular serine and glycine are abundant. In contrast, only PHGDH-expressing, aggressive TNBC BrM cells should proliferate under serine- and glycine-limiting conditions. Measurements of cell proliferation using an automated live-cell analysis platform confirmed that aggressive TNBC BrM cells proliferated in CSF and -Ser/-Gly media, whereas indolent TNBC BrM cells proliferated poorly in these conditions (Fig. 3B). These results reveal that extracellular serine and glycine availability modulate cancer cell dependence on glucose-derived serine synthesis.

If PHGDH was responsible for the differential proliferation rates of aggressive and indolent BrM cells, suppression of PHGDH should also inhibit aggressive TNBC BrM cell growth in CSF and -Ser/-Gly media. We depleted PHGDH using two independent shRNAs (sh*PHGDH* #1 and #2; Supplementary Fig. S3F) and determined their effects on both glucose-derived serine synthesis and cell proliferation. In plasma media, serine labeling fell by approximately 5-fold in PHGDH-depleted cells, but serine pools remained comparable with control hairpin (shCtrl) cells (Fig. 3C; Supplementary Fig. S3G and S3H). However, PHGDH suppression decreased serine pools by 30% to 50% in cells cultured in CSF or -Ser/-Gly media (Supplementary Fig. S3H). These results demonstrate that PHGDH is required to maintain serine pathway activity and cell proliferation in serine- and glycine-limiting conditions (Fig. 3D).

To ensure that this phenotype was due to the catalytic activity of PHGDH, we reconstituted PHGDH-depleted cells with catalytically active or inactive shRNA-resistant PHGDH (Supplementary Fig. S3I). Expression of catalytically active PHGDH restored glucose-derived serine production and cell proliferation in both CSF or -Ser/-Gly media, whereas expression of a catalytically inactive PHGDH mutant (D175N, R236K, H283A; Supplementary Fig. S3J) failed to restore serine synthesis (Fig. 3E; Supplementary Fig. S3K and S3L) and cell growth (Fig. 3F) in serine- and glycine-limited conditions. These results confirm that PHGDH activity promotes glucose-derived serine synthesis and enables cells to proliferate in serine- and glycine-limited environments, such as the brain.

### PHGDH Enables Brain Metastasis

Our *in vitro* findings demonstrate that serine synthesis is essential for cancer cell growth in microenvironments comparable to the brain interstitium. To determine whether PHGDH was necessary for brain metastasis *in vivo*, we injected aggressive TNBC BrM cells expressing either a nontargeting hairpin (shCtrl) or two independent PHGDH-targeting hairpins (sh*PHGDH* #1 and sh*PHGDH* #2) into the left ventricle of athymic nude mice, and monitored metastatic progression by bioluminescence imaging (BLI). PHGDH suppression decreased the burden of brain metastases and improved the survival of mice bearing brain metastases (Fig. 4A and B). The 12-day improvement in median survival in mice induced by PHGDH depletion is comparable to prior studies using similar models (10, 11, 14, 51). To determine whether PHGDH suppression attenuated brain metastasis formation in a different tumor type, we depleted PHGDH in a non-small cell lung adenocarcinoma (NSCLC) cell line (H1975, aggressive NSCLC BrM) and induced brain metastases by intracardiac injection. Consistent with our data in aggressive TNBC BrM cells, PHGDH depletion in aggressive NSCLC BrM cells also suppressed brain metastasis in mice and improved overall

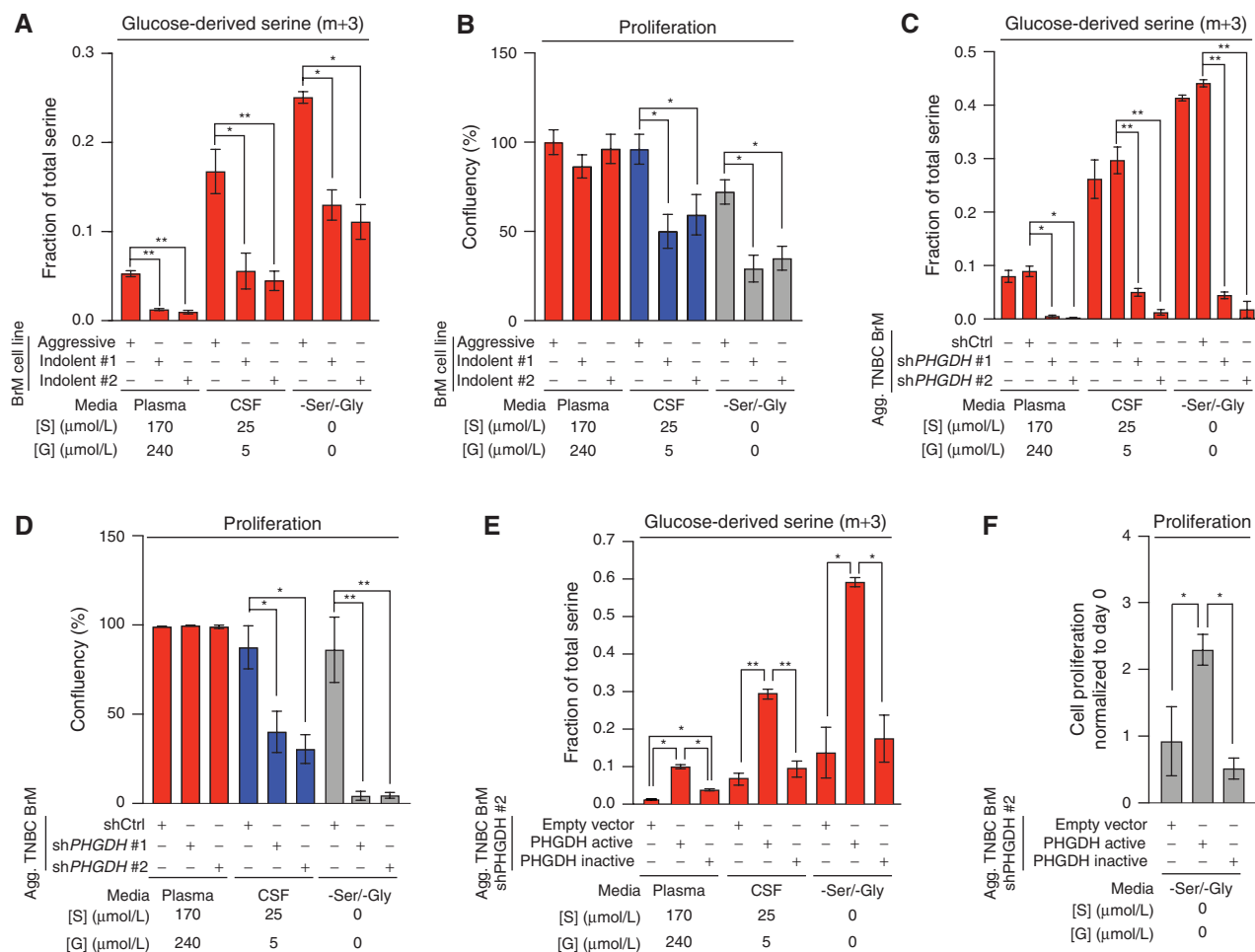


**Figure 3.** Aggressive TNBC brain metastases are serine prototrophs. **A**, Fractional labeling of intracellular U-<sup>13</sup>C-glucose-derived m+3 serine from aggressive or indolent brain metastatic cells grown in plasma, CSF, or -Ser/-Gly media. **B**, Proliferative capacity of aggressive or indolent TNBC BrM cells grown in plasma, CSF, or -Ser/-Gly media. **C**, Fractional labeling of intracellular U-<sup>13</sup>C-glucose-derived serine from aggressive brain-trophic cell lines expressing a control shRNA (shCtrl) or *PHGDH* shRNA (shPHGDH #1 or shPHGDH #2). **D**, Proliferative capacity of aggressive TNBC BrM cells expressing a control shRNA (shCtrl) or *PHGDH* shRNA (shPHGDH #1 or shPHGDH #2). **E**, Fractional labeling of intracellular U-<sup>13</sup>C-glucose-derived serine in aggressive TNBC BrM cells with a *PHGDH* shRNA (shPHGDH #2) expressing either an empty vector (EV) control, catalytically active or catalytically inactive, shRNA-resistant *PHGDH*. **F**, Proliferative capacity of *PHGDH* knockdown aggressive TNBC BrM cells with a *PHGDH* shRNA (shPHGDH #2) expressing either an empty vector (EV) control, catalytically active, or catalytically inactive, shRNA-resistant *PHGDH*. Cell proliferation data was monitored over 4 to 6 days using an Incucyte or Multisizer Coulter Counter. Error bars, SDs.

survival (Fig. 4C and D; Supplementary Fig. S4A). These data demonstrate that *PHGDH* suppression attenuates breast and lung cancer brain metastasis in mice.

To determine whether *PHGDH* was sufficient to promote brain metastasis, we injected mice with parental MDA-MB-231 TNBC cells that expressed catalytically active *PHGDH* or catalytically inactive *PHGDH* (Supplementary Fig. S4B). Parental MDA-MB-231 cells do not express *PHGDH* endogenously and do not exhibit brain tropism when inoculated into mice. Surprisingly, the expression of catalytically active *PHGDH* was sufficient to promote brain metastasis, whereas expression of catalytically inactive *PHGDH* or an empty vector control failed to increase brain metastasis formation significantly (Fig. 4E-G; Supplementary Fig. S4C). Notably, we did not observe bioluminescence signal in other organs, suggesting that *PHGDH* activity primarily potentiates brain metastasis.

Furthermore, tail-vein injection of parental MDA-MB-231 cells expressing catalytically active *PHGDH* exhibited a non-significant trend toward increased lung metastases (LuM) by BLI, but this was not confirmed by histology (Supplementary Fig. S4D and S4E). Moreover, suppression of *PHGDH* in our aggressive TNBC LuM model did not affect lung metastasis burden (Supplementary Fig. S4F). These observations support a model in which enhanced glucose-derived serine pathway activity promotes brain metastasis.

### Pharmacologic Inhibition of *PHGDH* Suppresses Cell Growth in Serine- and Glycine-Limited Environments

First-generation *PHGDH* inhibitors impede the growth of *PHGDH*-dependent primary tumors, but these tool compounds have moderate potency, with IC<sub>50</sub> values in the

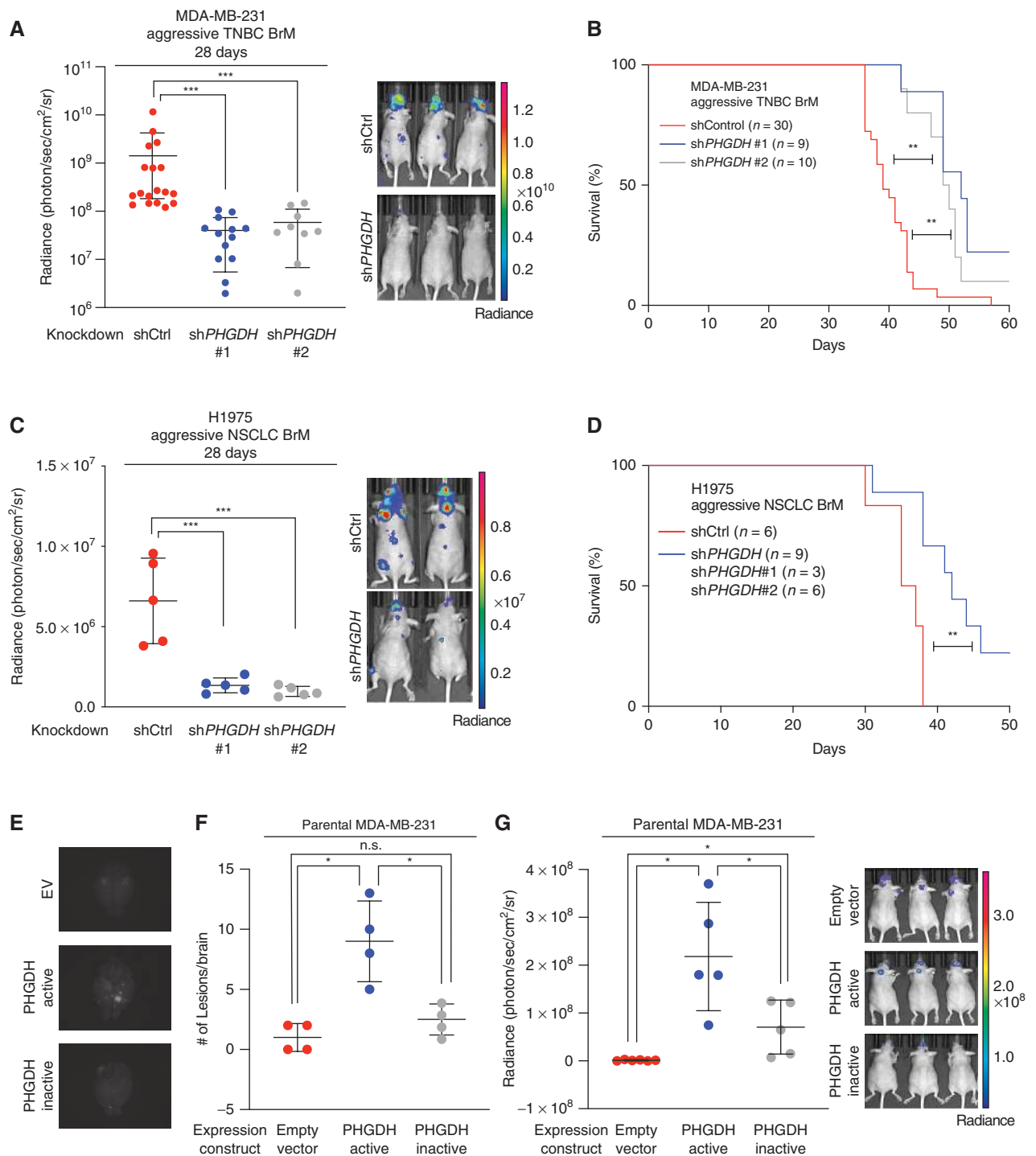


**Figure 4.** Genetic manipulation of PHGDH modulates brain metastasis. **A**, Radiance of brain metastasis-bearing mice measured at 28 days following intracardiac injection of aggressive TNBC BrM cells expressing either a control shRNA hairpin or shRNA hairpin targeting *PHGDH*. **B**, Kaplan-Meier plot showing disease-specific survival of mice injected with aggressive TNBC BrM cells expressing either a control shRNA (shCtrl) or *PHGDH* shRNA (shPHGDH #1 or shPHGDH #2). Significance was tested using the log-rank test. **C**, Radiance of brain metastasis-bearing mice measured at 28 days following intracardiac injection of NSCLC aggressive BrM cells expressing either a control shRNA hairpin or shRNA hairpin suppressing *PHGDH*. **D**, Kaplan-Meier plot showing disease-specific survival of mice injected with NSCLC aggressive BrM cells expressing either a control shRNA (shCtrl) or *PHGDH* shRNA (combined shPHGDH #1 and shPHGDH #2). Significance was tested using the log-rank test. **E**, Representative images of GFP-positive brain metastatic lesions derived from tumor-bearing mice injected with parental MDA-MB-231 cells expressing either an empty vector (EV) control, catalytically active *PHGDH*, or catalytically inactive *PHGDH*. **F**, Quantitation of brain metastases from parental MDA-MB-231 brain metastases by direct GFP visualization of isolated brains. **G**, Radiance of mice measured at 28 days following intracardiac injection with parental MDA-MB-231 cells expressing an empty vector control, catalytically active *PHGDH* or catalytically inactive *PHGDH*.



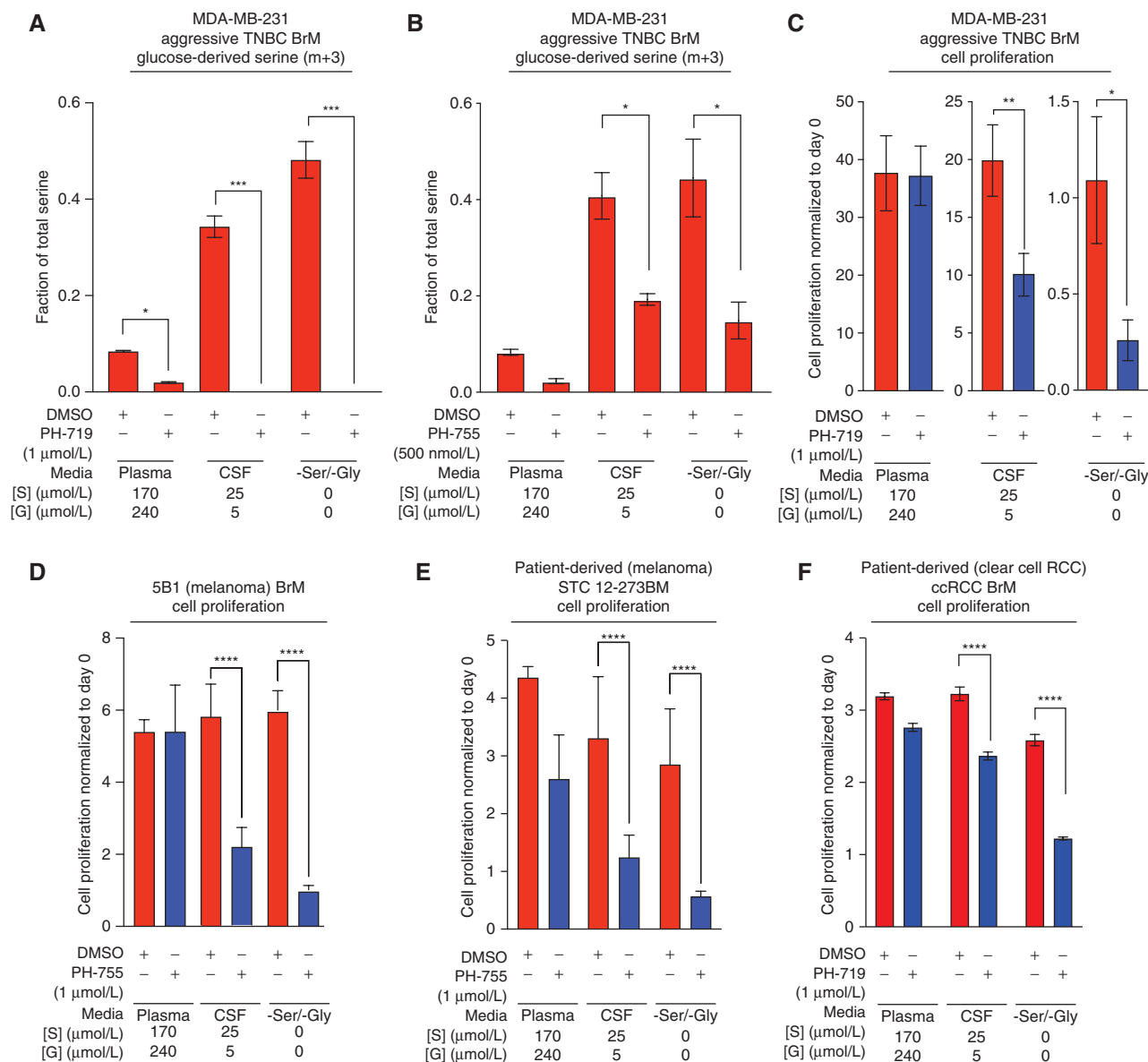


**Figure 5.** Pharmacologic inhibition of PHGDH decreases serine synthesis and cell proliferation. **A**, Fractional labeling of intracellular U-<sup>13</sup>C-glucose-derived m+3 serine from aggressive TNBC BrM cells treated with DMSO or 1  $\mu\text{mol/L}$  of the PHGDH inhibitor PH-719 in plasma, CSF, or -Ser/-Gly media. **B**, Fractional labeling of intracellular U-<sup>13</sup>C-glucose-derived m+3 serine from aggressive TNBC BrM cells treated with DMSO or 1  $\mu\text{mol/L}$  of the PHGDH inhibitor PH-755 in plasma, CSF, or -Ser/-Gly media. **C**, Proliferative capacity of aggressive TNBC BrM cells treated with DMSO or PH719 (1  $\mu\text{mol/L}$ ) in plasma, CSF, or -Ser/-Gly media. **D**, Anchorage-independent growth of 5B1 brain-trophic melanoma cells grown in plasma, CSF, or -Ser/-Gly media treated with DMSO (control; red bars) or 1  $\mu\text{mol/L}$  PH-755 (blue bars) for 5 days. **E**, Anchorage-independent proliferation of patient-derived short-term culture 12-273 melanoma brain metastasis (STC 12-273BM) melanoma cells grown in plasma, CSF, or -Ser/-Gly media treated with DMSO (control; red bars) or 1  $\mu\text{mol/L}$  PH-755 (blue bars) for 5 days. **F**, Proliferative capacity of patient-derived ccRCC BrM cells grown in plasma, CSF, or -Ser/-Gly media treated with DMSO (control; red bars) or 1  $\mu\text{mol/L}$  PH-719 (blue bars) for 5 days.

approximately 10  $\mu\text{mol/L}$  range. Second-generation PHGDH inhibitors have higher potency and improved pharmacokinetic and pharmacodynamic properties. Because PHGDH enzymatic activity is sufficient to promote brain metastasis *in vivo*, we tested second-generation PHGDH inhibitors in our models of brain metastasis.

PH-719 and PH-755 (Raze Therapeutics) are second-generation PHGDH inhibitors with nanomolar potency *in vitro* (52). Both PH-719 and PH-755 blocked glucose-derived

serine synthesis (Fig. 5A and B; Supplementary Fig. S5A and S5B) regardless of exogenous serine and glycine concentrations. However, both PH-719 and PH-755 inhibited the proliferation of aggressive TNBC BrM cells (Fig. 5C; Supplementary Fig. S5C), brain-trophic melanoma cells (Fig. 5D), patient-derived short-term culture (STC) 12-273 melanoma BrM cells (Fig. 5E), and patient-derived clear cell renal cell carcinoma BrM cells (ccRCC BrM; Fig. 5F) in serine- and glycine-limiting conditions. In addition, treatment of

four PHGDH-dependent cell lines (HT1080, HCC70, MDA-MB-468, and BT-20) and three melanoma cell lines (12-273, 5B1, and A2058) in dose-response assays with PH-719 or PH-755 demonstrated that PHGDH inhibitors had  $EC_{50}$  values for cell growth inhibition of 0.5 to 5  $\mu\text{mol/L}$  when cultured in CSF or  $-\text{Ser}/-\text{Gly}$  media (Supplementary Fig. S5D and S5E). In contrast, two PHGDH-independent cell lines (MDA-MB-231 and ZR-75-1) exhibited a 6- to 10-fold higher  $EC_{50}$  for PH-719 (Supplementary Fig. S5D). Moreover, PH-719 blocked invasion of aggressive TNBC BrM cells selectively in  $-\text{Ser}/-\text{Gly}$  media (Supplementary Fig. S5F). These results support the hypothesis that extracellular serine and glycine availability modulates cellular sensitivity to second-generation PHGDH inhibitors.

### Pharmacologic Inhibition of PHGDH Attenuates Brain Metastasis

PH-755 is orally bioavailable and has a >24-hour half-life in mice (Supplementary Fig. S6A). To evaluate the effect of PH-755 on established brain metastases *in vivo*, we seeded the brains of immunodeficient mice with aggressive TNBC BrM cells for 1.5 weeks before treatment with vehicle or PH-755 (300 mg/kg twice daily by oral gavage; Fig. 6A and B; Supplementary Fig. S6B). PH-755 treatment reduced brain metastatic burden and extended the survival of mice (Fig. 6A and B; Supplementary Fig. S6C and S6D). Interestingly, although PH-755 attenuated breast cancer brain metastasis, it failed to restrict tumor growth of aggressive TNBC BrM cells implanted into the mammary fat pad (Supplementary Fig. S6E). Moreover, PH-755 treatment impeded the progression of intracranially implanted patient-derived ccRCC BrM tumors (Fig. 6C). These data provide proof of concept that small-molecule PHGDH inhibition reduces the growth of established brain metastasis.

Prevention of brain metastasis would also benefit patients with cancers that have a high propensity to spread to the brain (53). To test whether prophylactic treatment with PHGDH inhibitors would attenuate brain metastasis formation, we administered PH-755 for 24 hours prior to left ventricular inoculation of aggressive TNBC brain metastatic cells into athymic nude mice. Prophylactic PH-755 treatment substantially increased metastasis-free survival and reduced brain metastasis burden compared with vehicle treatment (Fig. 6D and E; Supplementary Fig. S6F–S6H). Notably, the frequency and size of brain metastatic lesions were approximately 20 times greater in mice treated with vehicle than in mice treated with PH-755, and no metastases were identified in approximately 50% of the PH-755 treatment group (Fig. 6E; Supplementary Fig. S6I). Most impressively, prophylactic PH-755 treatment increased the overall survival of brain metastasis-bearing mice by a median of 21.5 days, with minimal lung and liver metastatic burden (Fig. 6F; Supplementary Fig. S7A). Notably, this survival benefit is greater than most other monotherapies tested in similar murine models of brain metastasis (10, 11).

To determine the pharmacodynamic consequences of serine synthesis inhibition, we quantified amino acid concentrations in the plasma and CSF of tumor-bearing mice treated with vehicle or PH-755. PH-755 lowered plasma and CSF serine concentrations, but did not affect the concentrations

of most other amino acids or metabolites (Supplementary Fig. S7B–S7E).  $U\text{-}^{13}\text{C}$ -glucose labeling of mice fasted for 6 hours revealed that PH-755 decreased glucose incorporation into serine in both the plasma and dissected brain metastases (Supplementary Fig. S7F–S7H). In addition, we used real-time metabolic imaging with hyperpolarized (HP) [ $1\text{-}^{13}\text{C}$ ] pyruvate to determine whether PH-755 treatment affected the dynamic rate of conversion of pyruvate to lactate in intracranially implanted aggressive TNBC BrM cells. The rate of conversion of pyruvate to lactate ( $k_{PL}$ ) measured 3 hours after PH-755 treatment was significantly decreased in TNBC BrM brain metastases in PH-755-treated mice compared with vehicle-treated mice (70%,  $P < 0.05$ ; Supplementary Fig. S7I). Mice treated with PH-755 did not lose weight during the 8-week treatment in spite of the potential systemic toxicities of inhibiting serine biosynthesis (Supplementary Fig. S7J). These data serve as proof of concept that PHGDH inhibitors might be useful in the treatment and prevention of brain metastases.

### PHGDH Inhibition in Serine- and Glycine-Limited Media Generates DNA Damage and Impedes Cell-Cycle Progression through Selective Nucleotide Depletion

To investigate the potential mechanisms responsible for reduced cell growth in serine-limited microenvironments following PHGDH inhibition, we performed comparative phospho-proteomics on PHGDH-depleted aggressive TNBC BrM cells cultured in plasma or  $-\text{Ser}/-\text{Gly}$  media. Unexpectedly, we found that PHGDH suppression selectively induced a substantial increase in phosphorylation of proteins involved in the DNA damage response. These proteins included, among others, 53BP1, RAD50, and H2A.X (Fig. 7A; Supplementary Fig. S8A). To confirm these findings pharmacologically, treatment of aggressive TNBC BrM cells with PH-719 induced 53BP1 and  $\gamma\text{H2A.X}$  foci formation selectively in cells cultured in  $-\text{Ser}/-\text{Gly}$  media, indicative of a DNA damage response (Fig. 7B and C; Supplementary Fig. S8B and S8C).

Because serine is the precursor of nucleotides that are needed for DNA synthesis, replication, and repair, we hypothesized that the selective induction of DNA damage may be a result of nucleotide depletion. To determine whether the selective induction of DNA damage by PHGDH inhibition resulted in reduced DNA synthesis and cell-cycle arrest, we treated aggressive TNBC BrM cells with PH-719, and determined cell-cycle profiles by FITC-BrdU incorporation, followed by flow cytometry. PHGDH inhibition in plasma media had little effect on cell-cycle distributions, but PHGDH inhibition in CSF and  $-\text{Ser}/-\text{Gly}$  media reduced overall labeling with BrdU, suggesting decreased nucleotide incorporation and potentially impaired replication fork elongation throughout the early, mid, and late S-phase cell cycle (Fig. 7D; Supplementary Fig. S8D). Intriguingly, although PHGDH inhibition under  $-\text{Ser}/-\text{Gly}$  conditions resulted in little or no BrdU incorporation in early S-phase, there appeared to be some evidence of replication during late S-phase, perhaps due to DNA repair. These results suggest that serine synthesis inhibition in conditions with low microenvironmental serine and glycine induces DNA damage and impedes cell-cycle progression.

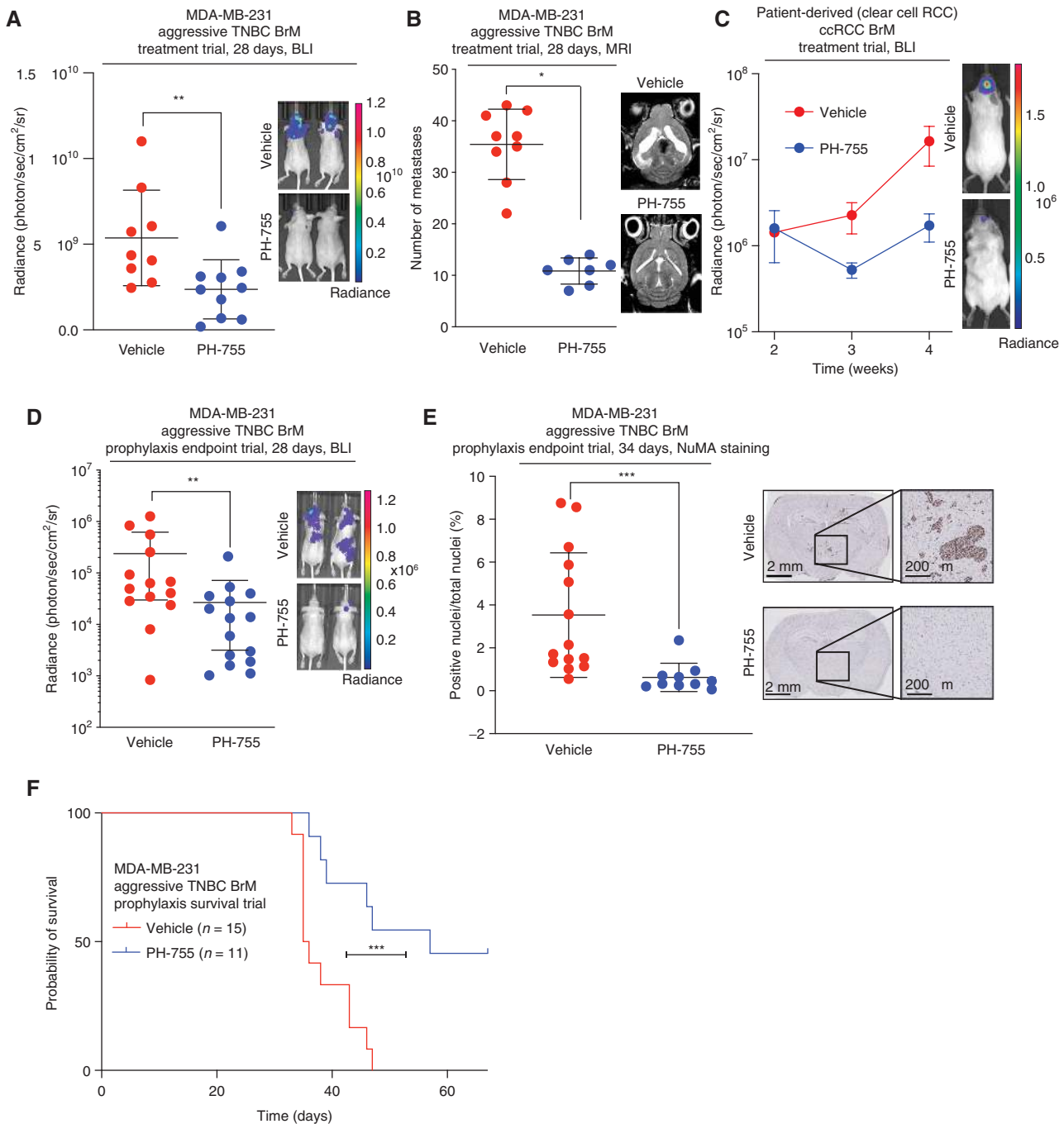


**Figure 6.** Pharmacologic inhibition of PHGDH attenuates brain metastasis. **A**, Radiance, measured at 28 days post-intracardiac injection, of aggressive TNBC BrM-bearing mice treated with vehicle or 300 mg/kg of PH-755 twice daily. Treatment began 1.5 weeks after the initial introduction of cancer cells into mice. **B**, Quantification of brain metastatic lesions by MRI from mice treated with vehicle control or 300 mg/kg of PH-755 twice daily. **C**, Radiance of RCC BrM patient-derived xenograft brain metastasis-bearing mice treated with vehicle or 300 mg/kg of PH-755 twice daily. Treatment began 2 weeks after the initial introduction of cancer cells into mice. Error bars, SEM. **D**, Radiance, measured at 28 days post-intracardiac injection, of aggressive TNBC BrM-bearing mice treated prophylactically with vehicle or 300 mg/kg PH-755 twice daily. **E**, Quantitation by IHC of human Nuclear Mitotic Apparatus (NuMA)-positive nuclei relative to total nuclei count, indicating the burden of brain metastases, from mice treated prophylactically with vehicle or PH-755. Tissue was harvested 34 days postinjection. **F**, Kaplan-Meier plot showing overall survival of mice treated prophylactically with vehicle or 300 mg/kg PH-755 twice daily.

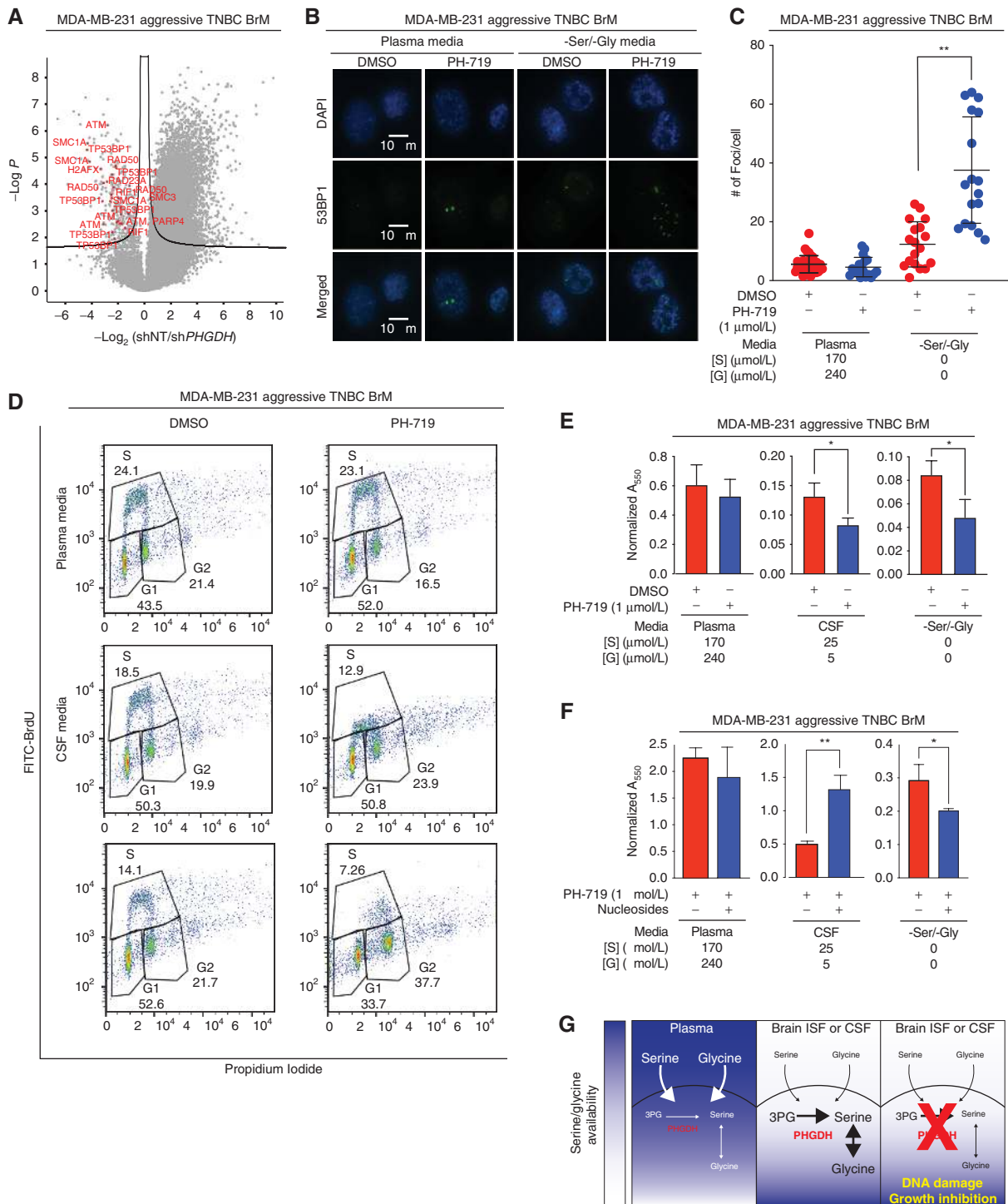


**Figure 7.** PHGDH inhibition promotes the DNA damage response in a low-serine environment. **A**, Volcano plot of the *P* value versus the log<sub>2</sub> phospho-protein abundance differences between aggressive BrM cells expressing a control shRNA or *PHGDH* shRNA cultured in *-Ser/-Gly* media (line: FDR < 0.05). Each dot represents a phosphorylation site. **B**, Immunofluorescence staining for 53BP1 foci in aggressive TNBC BrM cells treated with DMSO or the *PHGDH* inhibitor PH-719 in plasma or *-Ser/-Gly* media. **C**, Quantitation of 53BP1 foci per cell in **B**. **D**, Cell-cycle distribution of aggressive TNBC BrM cells cultured in plasma, CSF, or *-Ser/-Gly* media, and treated with DMSO or PH-719 for 12 to 16 hours. Cells were labeled with FITC-BrdU for 1 hour and stained with propidium iodide. **E**, Quantitation of colony formation assay of aggressive TNBC BrM cells in the absence or presence of PH-719 cultured in plasma, CSF, or *-Ser/-Gly* media. **F**, Quantitation of nucleoside rescue of TNBC BrM colony formation in the presence or absence of PH-719. **G**, Working model of brain metastasis sensitization to *PHGDH* inhibition. In the extracranial microenvironment, abundant exogenous serine and glycine compensate for inhibition of endogenous glucose-derived serine synthesis. The serine- and glycine-limited microenvironment of the brain imposes a metabolic dependency on serine and glycine synthesis, resulting in DNA damage and attenuation of brain metastasis progression when *PHGDH* is inhibited in brain metastases.

Downloaded from <http://aacrjournals.org/cancerdiscovery/article-pdf/10/9/1352/1818700/1352.pdf> by guest on 28 August 2022

To demonstrate that increased PHGDH expression in serine-limiting conditions promoted clonogenic survival, we overexpressed catalytically active or catalytically inactive PHGDH in parental MDA-MB-231 cells and carried out colony formation assays. Expression of catalytically active, but not catalytically inactive, PHGDH promoted colony formation in CSF and -Ser/-Gly media (Supplementary Fig. S8E). To determine whether PHGDH inhibition decreased clonogenic survival when exogenous serine and glycine were limiting, we carried out colony formation assays of aggressive TNBC BrM cells treated with PH-719. PHGDH inhibition significantly reduced aggressive TNBC BrM colony formation selectively in CSF and -Ser/-Gly media, but not in plasma media (Fig. 7E; Supplementary Fig. S8F). These data demonstrate that PHGDH activity is important for clonogenic cell survival when exogenous serine and glycine are limiting.

To delineate whether the selective DNA damage response due to PHGDH inhibition was caused by a reduction in serine and glycine incorporation into nucleotides, we performed metabolomics on U-<sup>13</sup>C-glucose-labeled cells where PHGDH activity was perturbed. Genetic depletion and pharmacologic inhibition of PHGDH depleted AMP and GMP pools in aggressive TNBC BrM cells when extracellular serine and glycine were limiting (Supplementary Fig. S9A–S9D). Interestingly, PHGDH inhibition or suppression did not perturb NAD:NADH ratios, but did reduce NADPH:NADP ratios in CSF or -Ser/-Gly media, suggesting a potential redox defect (Supplementary Fig. S9E–S9H). Ribose-5-phosphate pools slightly increased selectively following PHGDH inhibition, consistent with decreased incorporation into nucleotide synthesis (Supplementary Fig. S9I and S9J). Finally, nucleoside supplementation increased colony formation of aggressive TNBC BrM cells treated with PHGDH inhibitor in CSF media (Fig. 7F; Supplementary Fig. S9K), suggesting that nucleotide synthesis limited tumor cell growth when exogenous serine and glycine concentrations were low. Nucleosides did not rescue colony formation of cells growing in -Ser/-Gly media, likely due to the stress of colony formation when serine and glycine were absent.

PHGDH activity is important for mitochondrial redox homeostasis in hypoxia (54). To determine whether hypoxia limited cancer cell proliferation in limiting serine and glycine conditions, we grew aggressive TNBC BrM cells in normoxia (21% oxygen) and hypoxia (1% oxygen) in plasma, CSF, and -Ser/-Gly media. Hypoxia proportionally reduces aggressive brain metastatic cell proliferation in plasma and CSF media, suggesting that limited exogenous serine and glycine do not synergize with hypoxia to reduce aggressive TNBC BrM cell proliferation (Supplementary Fig. S9L). These data demonstrate that PHGDH inhibition, in CSF-like conditions, selectively depletes nucleotide pools and triggers a DNA damage response that results in delayed cell-cycle progression (Fig. 7G).

## DISCUSSION

Brain metastases arise from diverse primary tumors and are a major contributor to cancer mortality. We postulate that nutrient limitation in the brain microenvironment exerts a profound selection for cancer cells that efficiently synthesize serine. Using preclinical models of brain metastasis, we demonstrate that *de novo* glucose-derived serine synthesis

enables brain metastasis formation, and that small-molecule inhibitors of PHGDH reduce brain metastasis burden and improve overall survival in mice (Fig. 7G). Conceptually, these findings advance the notion that cancer cells from disparate origins may converge to adopt similar metabolic phenotypes in a given metastatic target tissue (10, 55–57). Whether other organ sites in addition to the brain, such as the lung, liver, or bone, impose unique metabolic dependencies will be worth exploring in future studies.

Our data demonstrate that interstitial rather than bulk tissue, serine, and glycine concentrations dictate brain metastasis dependence on serine synthesis and sensitivity to PHGDH inhibition. Microdialysis measurements of circulating serine and glycine levels in the adipose interstitium are 2 and 3 times higher than in the plasma, respectively, suggesting that these amino acids are not always limiting for primary breast tumors (23). This is consistent with the possibility that PHGDH is dispensable for primary tumor growth. Indeed, PHGDH is expressed in approximately 40% of primary human breast cancers (33, 36, 37). However, this subset of breast cancers with high PHGDH expression is associated with poorer survival and may have a higher propensity to metastasize to the brain. This also agrees with our hypothesis that PHGDH enables cancer cells to overcome the selection pressure imposed by the nutrient-limited environment of the brain, where serine concentrations are below the reported  $K_m$  values for the primary serine transporters ASCT1 and ASCT2 (Serine  $K_m \approx 56 \mu\text{mol/L}$ ; ref. 58).

Recent sequencing studies have found that primary tumors and brain metastases evolve independently and represent genetically distinct and divergent populations. These studies have led to the identification of several clinically relevant and actionable mutations in EGFR, ERBB2, CDK4/6, and the PI3K/AKT/mTOR pathway in brain metastases (16, 59, 60). In the recent HER2CLIMB trial, tucatinib, a small-molecule HER2 inhibitor, improved progression-free survival by 2.2 months in patients with brain metastases (61–63). In addition, combined immune checkpoint blockade with ipilimumab and nivolumab induced intracranial responses in up to 30% of patients with melanoma brain metastases (62). Although these promising data demonstrate intracranial efficacy of targeted therapies and immunotherapies, a substantial fraction of patients do not respond to these agents, making novel treatments for brain metastases an ongoing and significant unmet clinical need.

Copy-number alterations in *MYC*, *YAP1*, and *MMP13* have also been identified in patients with lung cancer brain metastases (60). Intriguingly, oncogenic mutations in *MYC* induce serine, glycine, and nucleotide biosynthesis by regulating the expression of SHMT2, which converts serine to glycine for folate and nucleotide synthesis (64–67). These findings suggest that *MYC* may drive metabolic adaptation to the brain microenvironment, and that SHMT1/2 inhibitors may also be useful for treating brain metastases (68–71).

PHGDH inhibitors may help treat brain metastases but will also inhibit *de novo* serine synthesis in nonmalignant proliferative and nonproliferative cells. Previous studies have shown that PHGDH is highly expressed in radial glial cells, antitumor CD8<sup>+</sup> T cells, Tregs, astrocytes, macrophages, and endothelial cells, all of which are dependent on functional

glucose-derived serine synthesis for their respective functions (52, 72–75). Interestingly, inhibition of serine synthesis in Tregs appears to inhibit Treg attenuation of immune responses and promote antitumor immunity (73). This suggests that inhibition of serine synthesis may not be exclusively immunosuppressive. In addition, humans with hypomorphic mutations in PHGDH exhibit developmental delays that can be ameliorated by serine supplementation, suggesting that transitory PHGDH inhibition following completion of neuronal development may be tolerable. Moreover, a recent study found that systemic depletion of PHGDH was well tolerated in multiple highly proliferative tissues in adult mice (76). These results suggest that PHGDH inhibitors may be well tolerated, provided that adequate serine and glycine are available in the diet. Although our study found no evidence of neurotoxicity or weight loss due to PHGDH inhibition, future studies will be needed to determine the side effects of PHGDH inhibition and its interactions with other cancer therapies—particularly radiotherapy, the primary treatment modality for brain metastases.

Ultimately, the development of novel therapies that target the cancer metabolic vulnerabilities will require a deep understanding of the interplay between intermediary metabolism and the cellular microenvironment. Although our current study does not examine the exchange of nutrients among tumor cells, astrocytes, and neurons, we recognize that this is a promising and exciting area of brain metastasis research.

Here, we demonstrate that metabolic constraints imposed by the nutrient-limited brain microenvironment confer brain metastasis dependency on serine synthesis. The tolerability and selective efficacy of second-generation PHGDH inhibitors provide proof-of-concept evidence that tailored antimetabolite therapy may complement existing treatment modalities and could improve the management of brain metastasis.

## METHODS

### Cell Culture and Media

Cells were grown in DMEM without glucose, glutamine, serine, glycine, and sodium pyruvate (US Biological D9802-01) or DMEM with L-glutamine and sodium bicarbonate, without glucose, serine, and glycine with 100 IU/mL penicillin and 100 µg/mL streptomycin. Serine and glycine were prepared as 100× DMEM stocks in water and sterile filtered. Glucose, glutamine, serine, and glycine were added to the media as needed. Melanoma short-term culture 12–273 brain metastasis (STC 12-273BM) was grown in DMEM as described above with an additional 1% (v/v) of MEM nonessential amino acids (Thermo Fisher Scientific, #11140076). A 100× amino acid stock and a nonessential amino acid mix lacking serine and glycine was prepared as a 50× stock and added to the media, along with serine and glycine as needed. Dialyzed inactivated FBS (dIFS) was added to all media to 10% (v/v), and the complete media were filtered through a 0.2-µm filter prior to use. Cells were grown in 10-cm dishes in a 5% CO<sub>2</sub>, ambient oxygen incubator and trypsinized when confluent (roughly every three days). Cell lines were authenticated by STR profiling (Duke DNA Analysis Facility, Durham, NC) and tested negative monthly for *Mycoplasma* by PCR.

### Knockdown and Overexpression Constructs

Luciferase expression was achieved using pLVX plasmid (expressing eGFP and luciferase; gift of E. Hernando, New York University Langone Health, New York, NY) and cells stably expressing luciferase

were sorted for eGFP expression. PHGDH expression was achieved using the pMXS retroviral expression system and pCW57.1 lentiviral expression system. Cells were selected using G418 (0.5 mg/mL) or puromycin (2 µg/mL), respectively. Stable knockdown of human PHGDH was achieved using shRNAs in pLKO as described previously (41). Two to 4 distinct shRNA hairpins were screened per target. shRNA sequences and TRC accession numbers are listed in Supplementary Table S1. shNT was obtained from Sigma-Aldrich (Mission SHC202). Catalytically inactive PHGDH constructs are available from Addgene as follows: pCW-codon optimized catalytically inactive PHGDH (154903) and pMXS catalytically inactive PHGDH (154906).

### Growth Curves

For growth curves, cells were grown for 4 to 6 days and counted using an Incucyte (Essen Biosciences) or a Z2 Coulter Counter (Beckman Coulter). For low-attachment growth assays, cells were seeded in 24-well plates (Corning CLS3473) in the appropriate media and counted using a Z2 Coulter Counter after 1 and 5 days. Small-molecule dose-response curves were printed using an D300e Digital Dispenser (HP Specialty Printing Systems) with DMSO <0.5% of the culture volume, and cell growth was measured by CellTiter-Glo (Promega) after 4 days. All plots, curve fitting, and statistical analysis were carried out with GraphPad Prism.

### Proteomic and Phospho-Proteomic Profiling

$2 \times 10^6$  cells were collected and washed three times with cold PBS before flash-freezing the samples in liquid nitrogen and shipping on dry ice. Control and brain metastases samples were thawed on ice and prepared following the in-stage tip sample preparation method with minor modifications (77). Briefly, 100 µL of the reducing alkylating sodium deoxycholate buffer (PreOmics) was added to the samples before protein denaturation at 100°C for 20 minutes. Samples were further homogenized by 15-minute sonication in a Biorupter (30 seconds on/off cycles, high settings). Proteins were then digested by Lys-C and trypsin overnight at 37°C on a shaker set at 1,200 rpm. Peptides were acidified to a final concentration of 0.1% trifluoroacetic acid (TFA) for SDB-RPS binding and desalted before LC/MS-MS analysis. Samples were measured on a Quadrupole Orbitrap Mass Spectrometer (Q Exactive HF, Thermo Fisher Scientific) coupled to an EASYnLC 1200 Ultra-High-Pressure System (Thermo Fisher Scientific) via a nano-electrospray ion source (78, 79). About 1 µg of peptides was loaded on a 40-cm HPLC column (75 µm inner diameter; in-house packed using ReproSil-Pur C18-AQ 1.9-µm silica beads; Dr Maisch GmbH, Germany). Peptides were separated using a linear gradient from 3% to 23% solvent B in 82 minutes and stepped up to 40% in 8 minutes at 350 nL per minute where solvent A was 0.1% formic acid in water and solvent B was 80% acetonitrile and 0.1% formic acid in water. The total duration of the gradient was 100 minutes. Column temperature was kept at 60°C by a Peltier element containing, in-house developed oven. The mass spectrometer was operated in top-15' data-dependent mode, collecting MS spectra in the Orbitrap mass analyzer (60,000 resolution, 300–1,650 m/z range) with an automatic gain control (AGC) target of 3E6 and a maximum ion injection time of 25 ms. The most intense ions from the full scan were isolated with a width of 1.4 m/z. Following higher energy collisional dissociation (HCD) with a normalized collision energy (NCE) of 27%, MS-MS spectra were collected in the Orbitrap (15,000 resolution) with an AGC target of 1E5 and a maximum ion injection time of 25 ms. Precursor dynamic exclusion was enabled with a duration of 20 seconds. Tandem mass spectra were searched against the 2015 Uniprot human databases (UP000005640\_9606 and UP000005640\_9606\_additional) using MaxQuant version 1.5.3.34 with a 1% FDR at the peptide and protein level, peptides with a minimum length of seven amino acids with carbamidomethylation as a fixed modification and protein

N-terminal acetylation and methionine oxidations as variable modifications (80). Enzyme specificity was set as C-terminal to arginine and lysine using trypsin as protease, and a maximum of two missed cleavages was allowed in the database search. The maximum initial mass tolerance for precursor and fragment ions was 4.5 ppm and 20 ppm, respectively. If applicable, peptide identifications by MS-MS were transferred between runs to minimize missing values for quantification with a 0.7-minute window after retention time alignment. Label-free quantification was performed with the MaxLFQ algorithm using a minimum ratio count of 1. Statistical and bioinformatics analysis was performed with Perseus software (version 1.5.5.0), Microsoft Excel, and R statistical software. Proteins that were identified in the decoy reverse database or only by site modification were not considered for data analysis. The median of technical triplicates (referring to independent sample preparations) was calculated and mean log<sub>2</sub> ratios of biological duplicates (two metastases and two control tissues collected at different locations of the pleural cavity) and the corresponding *P* values were visualized with volcano plots. We used *t* tests for binary comparisons and SAM with *s*<sub>0</sub> = 0.1 and an FDR < 0.05 or < 0.01 for the assessment of *t* test results in volcano plots. The FDR was corrected for multiple hypotheses based on permutation-based FDR correction. The mass spectrometry proteomics data have been deposited to the ProteomeXchange Consortium via the PRIDE partner repository with the dataset identifier PXD020532.

### Western Blotting

Tissue and cell lysates were prepared using RIPA buffer (Cell Signaling Technology) supplemented with protease inhibitor cocktail (Thermo Fisher Scientific). Protein concentrations were quantitated using Bio-Rad Protein Assay. Equal amounts of protein (10–30 µg) were separated on 4% to 12% Bolt bis-tris plus gels (Thermo Fisher Scientific) and transferred to Immobilon FL polyvinylidene difluoride membranes (Millipore Sigma), which were blocked in 5% milk in TBS-T at room temperature for 1 hour and incubated with primary antibodies at 4°C overnight. Blots were incubated with anti-mouse and anti-rabbit secondary antibodies conjugated to horseradish peroxidase (HRP; Cell Signaling Technology) at room temperature for 1 hour before visualization with Pierce ECL Western Blotting Substrate in a BioRad ChemiDoc Plus Imaging system. Blots were stripped with RestorePlus Western Blot Stripping Buffer (Thermo Fisher Scientific) prior to probing for the loading control.

The following primary antibodies were used: PHGDH (rabbit polyclonal, Sigma #HPA021241; rabbit mAb, Cell Signaling Technology – CST #66350), ERK2 (rabbit mAb, Abcam #ab32081); β-actin (mouse mAb, Abcam #ab8226; rabbit mAb, CST #8457); HSP90 (rabbit polyclonal, CST #4874); Rad50 Antibody (Rabbit polyclonal, CST #3427), Phospho-Rad50 (Ser635; Rabbit polyclonal, CST #14223), Phospho-ATM (Ser1981; D6H9, Rabbit mAb, CST #5883), and ATM (D2E2; Rabbit mAb, CST #2873).

### Immunofluorescence

Cells were fixed with ice-cold methanol for 15 minutes or 4% paraformaldehyde. Subsequently, cells were permeabilized and blocked with 2% BSA. Primary antibody was added at 1:500 in 1% TBST+1% BSA overnight at 4°C. After three washes with 1× PBS, secondary antibody was added at 1:400 with DAPI. After 30 minutes at room temperature, cells were mounted with Prolong Diamond Antifade Mount (Life Technologies). Antibodies used were: 53BP1 (rabbit polyclonal, Novus Biologicals #NB100-304), H2A.X (rabbit polyclonal, Bethyl Laboratories, #A300082A), and γH2A.X (rabbit polyclonal, phospho-S139; Abcam #ab2893).

### IHC

Clinical specimens were obtained and data handled under NYULMC Institutional Review Board (IRB) protocols i19-01549

and S16-00122. IHC was performed on 10% neutral buffered formalin fixed, paraffin-embedded human and murine tissue sections. Sections were collected at 5-µm onto plus slides (Thermo Fisher Scientific, catalog no. 22-042-924) and stored at room temperature prior to use. Unconjugated, polyclonal rabbit anti-human phosphoglycerate dehydrogenase (Sigma Aldrich catalog no. HPA021241 Lot# GR268490-13 RRID: AB\_10680001) was used for human tissues. Unconjugated, polyclonal rabbit anti-human Nuclear Mitotic Apparatus Protein (Abcam catalog no. 97585 Lot# B115626 RRID: AB\_1855299) was used for murine xenograft samples.

Chromogenic IHC was performed on a Ventana Medical Systems Discovery XT instrument with online deparaffinization and using Ventana's reagents and detection kits unless otherwise noted. Sections for PHGDH labeling were antigen retrieved in Ventana Cell Conditioner 2 (Citrate pH6.0) at 95°C for 20 minutes. Sections for NuMA were deparaffinized in xylene and rehydrated in graded ethanol followed by rinsing in deionized water. Epitope retrieval was performed in a 1,200-watt microwave oven at 100% power in 10 mmol/L sodium citrate buffer, pH 6.0 for 10 minutes. Slides were allowed to cool for 30 minutes, rinsed in distilled water, and loaded onto the instrument. Endogenous peroxidase activity was blocked with 3% hydrogen peroxide for 4 minutes. PHGDH antibody was diluted 1:100 in Ventana diluent (Ventana Discovery Antibody Diluent, catalog no. 760-108) and incubated for 3 hours at room temperature. NuMA was diluted 1:7,000 in Tris-BSA (25 mmol/L Tris, 15 mmol/L NaCl, 1% BSA, pH 7.2) and incubated for 12 hours. Both antibodies were detected with goat anti-rabbit HRP-conjugated multimer for 8 minutes. The immune complexes were visualized with 3,3'-diaminobenzidine and enhanced with copper sulfate. Slides were washed in distilled water, counterstained with hematoxylin, dehydrated, and mounted with permanent media. Appropriate positive and negative controls were run in parallel to study sections. Imaging was carried out with a Hamamatsu NanoZoomer whole-slide scanner.

For PHGDH scoring, the same board-certified pathologist (M. Snuderl) scored all PHGDH specimens in a blinded fashion for the intensity of PHGDH staining using a scale of 0–3, representing none, weak, moderate, and strong staining (36). PHGDH scoring for extracranial metastases was carried out by a board-certified pathologist (P. Cotzia) who reviewed the brain metastases for concordance. Data were analyzed using Fisher exact test. NuMA staining was quantitated by automated counting of positive and total nuclei using Visiopharm Image Analysis Software.

### Metabolite Profiling: Steady-State and Labeling Experiments

Cells were evenly seeded at 250,000 cells per well in a 6-well plate and allowed to attach for 24 hours. Prior to all labeling experiments, cells were pretreated with 1 µmol/L compound or the equivalent volume of DMSO in DMEM for 1 hour. For labeling experiments, U-<sup>13</sup>C-glucose (Cambridge Isotope Laboratories CLM-1396-PK) replaced the corresponding unlabeled glucose DMEM component. Cells were washed in 4°C 0.9%(w/v) NaCl in LC/MS-grade water and extracted in 1 mL/well of 3:1:2 methanol:water:chloroform with 500 nmol/L <sup>13</sup>C, <sup>15</sup>N-amino acids (Cambridge Isotope Laboratories MSK-A2-1.2) at internal extraction standards. The extraction solvent was dried in a SpeedVac and metabolite samples were stored at –80°C until analysis. Triplicate identically seeded and treated cells were trypsinized and analyzed with a Multisizer Coulter Counter (Beckman Coulter) to obtain cell counts and total cell volumes for normalization.

LC/MS analysis was carried out as described previously (40). In brief, metabolites were resuspended in 100 µL LC/MS-grade water and run on a SeQuant ZIC-pHILIC column (2.1 × 150 mm, 5 µm, Millipore-Sigma) on a Dionex UltiMate 3000 UPLC using a 0 to 80%

gradient of 20 mmol/L ammonium carbonate and 0.1% ammonium hydroxide, pH 9, in water. Mobile phase was introduced into the ionization source of a high-field Q Exactive Mass Spectrometer (QE HF; Thermo Fisher Scientific) running in polarity switching mode, and metabolites were identified by retention time, accurate mass, and fragmentation. Metabolite peaks were integrated with Skeleton (NYU Metabolomics Core Resource Laboratory) and normalized to internal standards and total cell volume. *m/z* ratios for <sup>13</sup>C-labeled metabolites were calculated using Skeleton and IsoMETLIN and corrected for isotopic abundance (81).

GC-MS analysis was carried out and analyzed as described previously (82). In brief, dried, extracted metabolites were derivatized using a MOX-tBDMCS method and analyzed by GC-MS using a DB-35MS column (30 m × 0.25 mm i.d., 0.25 μm) in an Agilent 7890B gas chromatograph interfaced with a 5977B mass spectrometer. Metabolites were identified by unique fragments and retention time in comparison with known standards. Peaks were picked in OpenChrom and integrated and corrected for natural isotopic abundance using in-house algorithms adapted from Fernandez and colleagues (83–85).

For glucose derivation, frozen and dried metabolites from the aqueous phase were dissolved in 50 μL of 2 wt% hydroxylamine hydrochloride in pyridine and incubated at 90°C for 1 hour. Next, 100 μL of propionic anhydride was added and the samples were picked at 60°C for 30 minutes. The samples were dried under nitrogen gas, resuspended in 100 μL of ethyl acetate, transferred to glass GC-MS vials, and capped prior to analysis.

### Animal Studies

Animal experiments were performed in accordance with protocols approved by the Weill Cornell Medicine, NYULMC, MIT, and MGH Institutional Animal Care and Use Committees (IACUC; Weill Cornell protocol 2013-0116; NYULMC protocol IA16-01862, MIT protocol 0119-001-22). For knockdown and inhibitor experiments, the minimum group size per arm was 12 for an anticipated difference of 55% between arms assuming a type I error probability of 0.05 and a power of 80%. We used 15 animals per arm in case of animal loss during intracardiac injection or subsequent procedures.

Intracardiac injection to induce brain metastases was performed as described previously (1). Briefly, cells were trypsinized and washed with PBS and  $1 \times 10^5$  cells (in 100 μL of PBS) were injected into the left cardiac ventricle of female 5- to 6-week-old athymic nude (nu/nu) mice (Jackson Laboratory strain 002019). Mice were then immediately injected with D-luciferin (150 mg/kg) and subjected to BLI using a IVIS Spectrum Xenogen instrument (Caliper Life Sciences) to ensure systemic dissemination of tumor cells. Metastatic burden was measured weekly after injection using BLI for up to 17 weeks. BLI images were analyzed using Living Image Software v.2.50. Disease-specific survival endpoints were met when the mice died or met the criteria for euthanasia under the IACUC protocol and had radiographic evidence of metastatic disease. T2 MR Imaging (0.5 mm slices) was obtained using a Bruker Biospec 94/30 USR 9.4 Tesla Small Animal MRI with a B-GA 20S gradient system in the MSKCC Rodent Imaging Core.

For orthotopic tumor implantation,  $2.5 \times 10^5$  cells in 100 μL of PBS were mixed 1:1 with Matrigel (BD Biosciences) and injected into the fourth mammary fat pad. Only one tumor was implanted per animal. Primary tumors were surgically excised when they reached approximately 1.5 cm in the largest dimension and metastatic dissemination was assessed using BLI imaging at 1- to 3-week intervals for up to 30 weeks. Distant metastasis-free survival endpoint was met when BLI signal was seen outside of site of primary tumor transplantation.

MFP and brain xenografts were generated in female nude mice of 8 to 9 weeks of age as described previously (86). Briefly, to generate

MFP tumors  $5 \times 10^6$  BT474 cells were resuspended in 50 μL of a 1:1 ratio of PBS and Matrigel Matrix, High Concentration (BD Biosciences, 354248). For brain tumors,  $1 \times 10^5$  BT474 cells were diluted in 1 μL of PBS and stereotactically injected into the left frontal lobe of the mouse brain. The day before implantation of tumor cells, a 0.36-mg or 0.72-mg 17β-estradiol pellet (Innovative Research of America, SE121) was implanted subcutaneously.

To derive short-term cultures from primary tumors and metastases, animals were imaged then sacrificed. *Ex vivo* BLI was subsequently performed on harvested organs to define the precise location of the metastatic lesion. Primary tumors and metastases were subsequently mechanically dissociated, cultured in DMEM, and sorted for eGFP to exclude host cells.

PH-755 was administered to mice to a dose of 300 mg/kg twice daily by oral gavage as a suspension in PBS containing 0.5% methylcellulose and 0.5% Tween 80. For brain histology, mice were deeply anesthetized with isoflurane and perfused with 10% formalin in PBS prior to sacrifice. Brains were harvested and fixed for 24 hours in 10% formalin followed by 48 hours in 70% ethanol, sectioned, and embedded for hematoxylin and eosin staining. Data represent the mean of two independent observers using FIJI to measure brain and metastasis size.

CSF was isolated as described previously (11). Whole blood was obtained by cardiac puncture into heparinized collection tubes (BD Microtainer), which were centrifuged at  $1,000 \times g$  at 4°C for 10 minutes. The plasma was flash-frozen until analysis. For LC/MS analysis, 20 μL of plasma was extracted with 80 μL 80:20 methanol:water with 500 nmol/L <sup>13</sup>C, <sup>15</sup>N-amino acids (Cambridge Isotope Laboratories MSK-A2-1.2) as internal extraction standards and centrifuged at  $15,000 \times g$  at 4°C for 10 minutes. The supernatant was dried in a SpeedVac and stored at -80°C until GC-MS or LC/MS analysis.

Differences in luminescence and in metastasis area were analyzed using the Mann-Whitney *U* test. Kaplan-Meier survival curves were compared using the log-rank test.

### Glucose Infusions in Mice

Catheters were surgically implanted into the jugular vein of tumor-bearing animals three days before the infusion experiment. Prior to the initiation of the study, mice were fasted for 6 hours. U-<sup>13</sup>C-glucose (Cambridge Isotope Laboratories) was infused at a constant rate of 30 mg/kg/minute for 12 hours into conscious, free-moving animals, after which the animals were terminally anesthetized with 120 mg/kg sodium pentobarbital. Blood was collected immediately by cardiac puncture, and tumors were harvested quickly, within 5 minutes of sacrifice. Tissues were frozen using a BioSqueezer (BioSpec Products) and stored at -80°C for subsequent metabolite extraction and analysis.

### Tissue GC-MS Measurements

Tissues were harvested quickly, rapidly crushed, and frozen using a BioSqueezer, and 10 to 30 mg of tissue was weighed out for extraction. Metabolites were extracted using ice-cold HPLC-grade methanol, water, and chloroform at a volume ratio of 600:300:400 (usually 600 μL:300 μL:400 μL). Samples were vortexed for 10 minutes at 4°C and centrifuged for 10 minutes at  $21,000 \times g$  and 4°C to separate the top, aqueous layer and the bottom, organic layer. Each layer was collected and dried under nitrogen gas and stored at -80°C for subsequent analysis by liquid or GC-MS.

### Pharmacokinetic and Pharmacodynamic Measurements

For *in vivo* labeling, mice were fasted for 6 hours starting from midnight and injected intraperitoneally with 2 g/kg of U-<sup>13</sup>C-glucose and sacrificed 60 minutes later. Following cardiac puncture to recover plasma, the brain was removed and visualized using a Leica M205 FA fluorescence stereo dissecting scope and metastases dissected quickly using a scalpel and forceps. Tissues were



quenched at liquid nitrogen temperatures using a BioSqueezer (BioSpec Products) and stored at  $-80^{\circ}\text{C}$ . Tissue samples were weighed, extracted in 200  $\mu\text{L}$  3:1:2 methanol:water:chloroform/mg of tissue, and the polar fraction was recovered, dried on a speedvac, and stored at  $-80^{\circ}\text{C}$  until LC/MS analysis or derivatization for GC-MS analysis.

Pharmacokinetic data were obtained from groups of  $n \geq 3$  mice that were administered PH-755 by oral gavage in suspension at the indicated doses, and whole blood was drawn and plasma was isolated at the indicated timepoints. PH-755 was quantitated by LC/MS using a standard curve.

### Cell-Cycle Analysis

Cells were treated with DMSO or PH-719 for 12 hours prior to the addition of BrdU at a final concentration of 10  $\mu\text{mol/L}$ . After 2 hours of BrdU labeling, cells were collected and fixed in 70% ethanol. Subsequently, ethanol-suspended cells were centrifuged at  $200 \times g$  for 5 minutes. The ethanol was removed and the cell pellet was suspended in 5 mL 1 $\times$  PBS before centrifuge at  $200 \times g$  for 5 minutes. Excess PBS was removed, and 100  $\mu\text{L}$  of staining buffer containing anti-BrdU-FITC was added and allowed to incubate for 1 hour at room temperature. Nine hundred microliters of DAPI solution (1:1,000) was added and incubated for 40 minutes in the dark room at room temperature. Approximately  $2 \times 10^6$  cells were sorted using a FACScalibur (BD Biosciences) flow cytometer. Results were analyzed using FlowJo (FlowJo, LLC).

### In Vitro Invasion Assay

For the invasion and migration assays, we used the Cytoselect Cell Invasion (CBA-110) kit. In brief,  $5 \times 10^4$  cells were suspended in serum-free medium and placed on top of the membrane. Medium containing serum was placed at the bottom. PHGDH inhibitor or vehicle, if needed, were added to both the top and bottom compartments. Cells that had invaded to the inferior surface of the collagen membrane were stained with crystal violet and counted 24 hours later.

### Colony Formation Assay

Aggressive brain metastatic cells were counted and seeded at 400 cells/well in a standard 6-well plate (Nunc) in full media. The media were exchanged on the following day and PHGDH inhibitors or DMSO were added. Sigma EmbryoMax Nucleosides purchased as a 100 $\times$  stock were diluted to 1 $\times$  for rescue experiments. Cells were incubated for 10 days, fixed with 10% formalin, and stained with crystal violet. After photography, the crystal violet was quantitated by dissolving in 500  $\mu\text{L}$  of 10% acetic acid and absorbance measured at 590 nm. Data were normalized to plating efficiency as measured by  $A_{590}$  24 hours after plating.

### Isolation of Patient-Derived CTCs

Patient-derived CTCs used in this study (BrX50 CTC line) were reported previously (87, 88). In brief, peripheral blood from patients with metastatic breast cancer were processed by CTC-iChip. CD45/CD15 conjugated magnetic beads were used to deplete white blood cells, and antibody agnostic CTCs were collected in the effluent. These CTCs were cultured in 4% oxygen, in RPMI with bFGF, EGF, and B27 supplementation. Once CTCs proliferated to have enough biological material for *in vivo* work, they were transduced with a GFP-luciferase expressing construct and injected by intracardiac injection into NSG mice. These mice were followed for 5 to 8 months for metastatic relapse by bioluminescence imaging. At endpoint, metastatic lesions were resected and sorted for GFP $^{+}$  cells. To obtain second-generation and third-generation brain metastatic derivatives, cells were expanded in culture, and additional rounds of *in vivo* injection ( $\sim 100\text{K}$  cells/mouse) were performed.

### Generation of RCC Patient-Derived Xenograft Model

A patient-derived xenograft (PDX) model of human renal cell carcinoma brain metastasis was generated by transplanting freshly obtained surgically excised tumor specimens from patients who had given consent under the IRB-approved protocol (MSKCC IRB #O6-107) into female immunocompromised NOD/SCID/IL2R $\gamma^{\text{null}}$  (NSG) mice (Jackson Laboratories strain 005557) subcutaneously. All relevant IRB and ethical regulations were followed (MSKCC IRB # 17-067). Tumors were maintained till the tumor size reached around 1.5 cubic cm each for a maximum of three serial passages. In brief, half of the freshly obtained tumor tissue (about 200–400 mg bulk) was cut into 4–8 mm pieces and directly retransplanted subcutaneously for passaging. The other half was minced into 2–4 mm pieces in serum-free MEM with nonessential amino acids (catalog no. 41500018, Thermo Fisher Scientific), transiently transduced with a lentiviral vector expressing pUltra-Chili-Luc plasmid (Addgene plasmid: 48688), and retransplanted into mice subcutaneously. To generate PDX-derived cell lines, the PDX tumor was chopped into 1–2 mm $^3$  pieces and incubated in Accutase (AT104; Innovative Cell Technologies) for cell detachment and separation over 1 to 2 hours. The dissociated tissues were sieved through 100- $\mu\text{m}$  cell strainers and the cells were pelleted by centrifugation at 1,200 rpm (Eppendorf Centrifuge 5810 R). The pellets were washed and resuspended in the RPMI buffer with 10% FBS including penicillin/streptomycin antibiotic cocktail for generating the primary PDX-derived cells. All the above sources of the PDX tumor were verified to form tumor subcutaneously and orthotopically at the primary kidney site as well as at the other metastatic sites such as lung and brain. Typically, PDX tumor growth became palpably evident during the first 2 to 4 weeks after engraftment, and tumors were harvested after an additional 4 to 8 weeks of growth following institutional Research Animal Resource Center (RARC)-supervised and IACUC-approved animal protocol. Primary tumor growth and metastases were followed using BLI or spectrum CT imaging.

### RNA Sequencing

HTSeq-count (v0.9.1) tool was applied with its default settings to count uniquely aligned reads from 77 RNA-sequencing (RNA-seq) BAM files downloaded from the European Genome-Phenome Archive (EGA; accession number EGAS00001003672). G.M. Fischer and M.A. Davies provided raw expected counts acquired from A375, MEWO, and WM1361A intracranial (ICr;  $n = 3$  each) and subcutaneous (SQ;  $n = 3$  each) xenografts as described previously. For all analyses, counts were normalized using the TMM method and generalized linear models were used for differential expression analyses. Comparisons of interest were performed using functions from the *edgeR* and *limma/voom* Bioconductor packages in R (v3.6.1). Low-expressed genes were filtered as follows: *filterByExpr* function for clinical samples and genes with an average  $\log_2(\text{CPM}+0.5) < 0$  for A375, MEWO, and WM1361A ICr and SQ xenografts. Blocking was performed to account for differences in patients or cell lines.

Pathways were assessed between ICr and SQ xenografts and between 35 melanoma brain metastases (MBM) and 42 patient-matched extracranial metastases (ECM) from multiple accession sites using the R package *fy* on default settings. The voom-transformed expression matrices were used as the initial inputs, and the GO gene set “GO:0006564; L-Serine Biosynthetic Processes” was used in comparisons. In parallel, a preranked gene set enrichment analysis (GSEA-P) was implemented on the clinical samples using the GenePattern module *GSEAPreranked* (v6.0.10). Gene sets featured 70 previously characterized KEGG metabolic pathways included in a single. gmt file. Rank metric was calculated as the sign of  $\log_2\text{-FCs}$  multiplied by the inverse of  $P$  values calculated using the *edgeR/limma/voom* pipeline. GSEA-P was performed on the rank metric-sorted list of genes using the “classic” Kolmogorov-Smirnov scoring scheme. Finally, site-specific

pathway analyses were performed between 4 MBMs and 5 patient-matched lung metastases; 12 MBMs and 12 patient-matched skin metastases; and 15 MBMs and 17 patient-matched skin/lung metastases using the *fy* package with the above-mentioned settings.

### In Vitro enzyme Activity

The D175N, R236K, H283A catalytically inactive mutant of PHGDH was constructed by overlapping PCR. N-terminally 6xHis tagged wild-type and catalytically inactive PHGDH were expressed, purified, and assayed as described previously (40).

### Hyperpolarization Using DNP and MRS Acquisition

A thirty-five-microliter mixture of [ $^{1-13}\text{C}$ ] pyruvate (14.2 mol/L, GE Healthcare) and GE trityl radical (15 mmol/L, GE Healthcare) was hyperpolarized by the DNP method using a SPINlab polarizer (5 T, 0.80 K, GE Healthcare). Following polarization for 3 hours, the frozen sample was rapidly dissolved in TRI buffer (10 mL, 100 mmol/L, pH 7.4) containing 1 mmol/L EDTA (Thermo Fisher Scientific) in  $\text{D}_2\text{O}$  (Cambridge Isotope Laboratories). The solution was neutralized in a receiving flask containing sodium hydroxide (10 N) such that the final solution was pH 7.4. 250  $\mu\text{L}$  of 100 mmol/L hyperpolarized [ $^{1-13}\text{C}$ ] pyruvate was injected intravenously in the tail vein of a catheterized animal in 10 seconds (89). HP pyruvate was injected at a concentration that saturates monocarboxylate transporter 1 (MCT1; pyruvate  $K_m = 2.14$  mmol/L; ref. 90). Immediately after completion of the HP pyruvate injection,  $^{13}\text{C}$  data were acquired using a 3T MRI system (Bruker) using a  $^1\text{H}/^{13}\text{C}$  volume RF coil;  $\text{T}_2$ -TurboRare images were acquired for anatomic localization, covering the whole tumor (TE/TR = 79.46/3570.6 ms, rare factor = 8,  $30 \times 40 \times 14$  of FOV, with thickness of 2 mm for slices). A preliminary dynamic slab study on a small group of mock mice was performed ( $n = 3$ ). The mock model was generated with stereotactic injection of 2  $\mu\text{L}$  of normal saline into their brain 3 weeks before imaging experiment. An axial two-dimensional echo-planar spectroscopic imaging (2DEPSI) sequence was used to acquire the HP spectra (80 mm  $\times$  40 mm FOV, 10-mm slab thickness, sweep width = 3,125 Hz, spectral points = 256, echo time = 4.84 ms, repetition time = 312.5 ms, flip angle  $12^\circ$ ), with the timing derived from the previous dynamic studies on mock mice. Three mice with orthotopic brain tumors were used [each mouse was treated with vehicle via oral gavage and 3 hours later was imaged, right after imaging the same mouse treated with PHGDHi (200 mg/kg) and 3 hours later was imaged], resulting in 4 tumor replicates per group. Spectroscopic data were processed using custom software to generate 2-D dynamic datasets registered to the corresponding anatomic MRI (MATLAB R2018a, Mathworks; ref. 91). The HP [ $^{1-13}\text{C}$ ]pyruvate signal (PYR) and [ $^{1-13}\text{C}$ ]lactate signal (LAC) were calculated from the area under the respective peaks for each voxel. The dynamic curves were then fit to a two-site exchange model to derive the rate constant  $k_{pb}$ , which represents the conversion rate of pyruvate to lactate, using open source software (SIVIC; ref. 92). The  $T_1$  of HP [ $^{1-13}\text{C}$ ] pyruvate was measured using a 1 Tesla Spinsolve Spectrometer approximately 147.0 ( $\pm 7$ s) (Magritek) with a 5 mm  $^1\text{H}/^{13}\text{C}$  coil as described previously (93).

### Disclosure of Potential Conflicts of Interest

B. Ngo reports grants from NCI and grants from NSF during the conduct of the study. J. Ni reports personal fees from Geode Therapeutics (consulting) outside the submitted work. S.F. Bakhom reports personal fees and other funding from Volastra Therapeutics Inc. (consultant, scientific advisory board, board of directors, founder equity) and personal fees from Sanofi (consulting) outside the submitted work. A. Friedman reports other funding from Raze Therapeutics, Inc. (equity holder) during the conduct of the study; and other funding from Raze Therapeutics (equity holder) outside the submitted work. M. Manfredi reports equity in a company that is developing one of the compounds in this publication. M. Yu reports

grants from NIH, Donald E. And Delia B. Baxter Foundation, Stop Cancer Foundation, Wright Foundation, and Pew Charitable Trusts during the conduct of the study; and nonfinancial support from CanTraCer Biosciences M. Yu is the founder and president for CanTraCer Biosciences and reports personal fees from Microsensor Labs (paid consultant) outside the submitted work. J.J. Zhao reports grants from NCI, DoD, and Breast Cancer Research Foundation during the conduct of the study; in addition, J.J. Zhao has a patent for DFCI 2103.001 pending; and is a cofounder and director of Crimson BioPharm Inc. and Geode Therapeutics Inc. R.K. Jain reports grants from NIH (R35-CA197742, R01-CA208205, U01-CA224173 and P01-CA080124), grants from National Foundation for Cancer Research, grants from The Ludwig Center at Harvard, grants from The Jane's Trust Foundation, grants from The Advanced Medical Research Foundation, and grants from Koch Institute/DFHCC Bridge Grant during the conduct of the study; personal fees from Amgen (honorarium), Chugai (consultant fees), Ophthotech (consultant fees), Merck (consultant fees), SPARC (consultant fees), SynDevRx (consultant fees & equity), XTuit (consultant fees & equity), Enlight (equity), Accurius Therapeutics (member, scientific advisory board), Tekla Healthcare Investors (boards of Trustees), Tekla Life Sciences Investors (boards of trustees), Tekla Healthcare Opportunities Fund (boards of trustees), and Tekla World Healthcare Fund (boards of trustees) outside the submitted work. K.R. Keshari reports grants from NIH and grants from STARR Cancer Consortium during the conduct of the study; and personal fees from nVision imaging Technologies (scientific advisory board member) outside the submitted work. M.A. Davies reports grants from AstraZeneca, grants and personal fees from Roche/Genentech and Sanofi-Aventis; and personal fees from Novartis, Array, and BMS outside the submitted work. M.G. Vander Heiden reports personal fees from Agios Pharmaceuticals (scientific advisory board), iTeos Therapeutics (scientific advisory board), Aeglea Biotherapeutics (scientific advisory board), and Auron Therapeutics (scientific advisory board) outside the submitted work. L.C. Cantley reports grants from the NCI, Breast Cancer Research Foundation, and The Gray Family Foundation during the conduct of the study; and personal fees from Petra Pharmaceuticals (founder and SAB and support for Cantley lab) and Volastra Pharmaceuticals (founder and SAB), and personal fees from Faeth (founder and SAB) outside the submitted work; in addition, L.C. Cantley has a patent for Docket 7252 pending (patent on PHGDH inhibitor not used in this study). M.E. Pacold reports grants from NCI, Mary Kay Foundation, Shifrin-Myers Breast Cancer Discovery Fund, V Foundation, NYU Melanoma SPORE, Melanoma Research Alliance, and John and Elaine Kanas Family Foundation during the conduct of the study; nonfinancial support and other from Raze Therapeutics (options); and personal fees from Thermo Fisher Scientific (travel funds) outside the submitted work; in addition, M.E. Pacold has a patent for US20180105508A1 issued, licensed, and with royalties paid from Raze Therapeutics (NCT-503, an earlier generation PHGDH inhibitor). M.E. Pacold is a consultant to and holds equity in Raze Therapeutics and is the recipient of travel funds from Thermo Fisher Scientific. Raze Therapeutics holds patents on compounds used in this work. No potential conflicts of interest were disclosed by other authors.

One of the Editors-in-Chief is an author on this article. In keeping with the AACR's editorial policy, the peer review of this submission was managed by a member of *Cancer Discovery's* Board of Scientific Editors, who rendered the final decision concerning acceptability.

### Authors' Contributions

**B. Ngo:** Conceptualization, data curation, formal analysis, validation, investigation, methodology, writing-original draft, writing-review and editing. **E. Kim:** Data curation, formal analysis, investigation, visualization, methodology, writing-review and editing. **V. Osorio-Vasquez:** Data curation, formal analysis, investigation,

visualization, methodology, writing-review and editing. **S. Doll:** Data curation, formal analysis, investigation. **S. Bustraan:** Data curation, formal analysis, investigation. **R.J. Liang:** Investigation. **A. Luengo:** Investigation. **S.M. Davidson:** Investigation, methodology. **A. Ali:** Formal analysis, investigation, visualization. **G.B. Ferraro:** Formal analysis, investigation. **G.M. Fischer:** Resources, data curation, formal analysis, investigation, visualization. **R. Eskandari:** Investigation. **D.S. Kang:** Resources, investigation. **J. Ni:** Formal analysis, investigation. **A. Plasger:** investigation. **V.K. Rajasekhar:** Investigation. **E.R. Kastenhuber:** Formal analysis, validation, investigation. **S. Bacha:** Investigation. **R.K. Sriram:** Investigation. **B.D. Stein:** Investigation. **S.F. Bakhoun:** Resources. **M. Snuderl:** Resources, investigation. **P. Cotzia:** Resources, investigation. **J.H. Healey:** Resources. **N. Mainolfi:** Resources. **V. Suri:** Resources. **A. Friedman:** Resources. **M. Manfredi:** Resources. **D.M. Sabatini:** Resources. **D.R. Jones:** Resources, formal analysis, validation, investigation. **M. Yu:** Resources, investigation. **J.J. Zhao:** Resources, investigation. **R.K. Jain:** Resources. **K.R. Keshari:** Resources, formal analysis, investigation. **M.A. Davies:** Resources, data curation. **M.G. Vander Heiden:** Resources, data curation, formal analysis, investigation, visualization. **E. Hernando:** Resources, supervision. **M. Mann:** resources, formal analysis, supervision. **L.C. Cantley:** Conceptualization, resources, supervision, funding acquisition, visualization, writing-review and editing. **M.E. Pacold:** Conceptualization, resources, data curation, formal analysis, supervision, funding acquisition, validation, investigation, visualization, methodology, writing-original draft, writing-review and editing.

## Acknowledgments

B. Ngo is supported by a National Science Foundation (NSF) Graduate Research Fellowship and the NCI of the NIH under the F99/K00 Career Transition Fellowship (F99CA234950). V. Osorio-Vasquez is supported by an NIH F31 Ruth L. Kirschstein National Research Service Award (NRSA) Pre-doctoral Fellowship (F31 CA250364-01). A. Luengo and S.M. Davidson were supported by an NSF Graduate Research Fellowship and T32GM007287. A. Ali is supported by the HHMI Medical Fellows Program. R. Eskandari is supported by a Tow Foundation Postdoctoral Fellowship from the Center for Molecular Imaging and Nanotechnology (CMINT) at Memorial Sloan Kettering. G.M. Fischer received research funding from the NIH National Center for Advancing Translational Sciences (TL1TR000369 and UL1TR000371) and The University of Texas MD Anderson Cancer Center (MD Anderson)/UTHealth Graduate School of Biomedical Sciences' Caroline Ross Fellowship, Schissler Foundation Fellowship, and Presidents' Research Scholarship. J.H. Healey and V.K. Rajasekhar are supported by the MSKCC NIH/NCI Cancer Center Support Core Grant P30-CA008748. S.F. Bakhoun is supported by the NIH (DP5OD026395 High-Risk High-Reward Program), the Department of Defense Breast Cancer Research Breakthrough Award W81XWH-16-1-0315 (project: BC151244), the Burroughs Wellcome Fund Career Award for Medical Scientists, the Parker Institute for Immunotherapy at MSKCC, the Josie Robertson Foundation, and the MSKCC core grant P30-CA008748. M. Yu is supported by an NCI K22 Career Transition Award (K22 CA175228-01A1), NIH DP2 award (DP2 CA206653), Donald E. And Delia B. Baxter Foundation, Stop Cancer Foundation, and Wright Foundation, and is a Pew-Stewart Scholar for Cancer Research. J.J. Zhao is supported by the NIH (R35 CA210057, P50 CA168504), DoD (W81XWH-18-1-0491), and the Breast Cancer Research Foundation. D.M. Sabatini is supported by the NCI of the NIH under Award R03 DA034602-01A1, R01 CA129105, R01 CA103866, and R37 AI047389. D.M. Sabatini is an investigator of the Howard Hughes Medical Institute. K.R. Keshari is supported by the NIH (R01CA237466, R01CA252037, and R21CA212958) and the STARR Cancer Consortium. M.A. Davies is supported by the Dr. Miriam and Sheldon G. Adelson Medical Research Foundation, the AIM at Melanoma Foundation, the NIH/NCI (R01 CA121118-06A1 and 2T32CA009666-21), the Cancer Prevention Research Institute of

Texas (CPRIT; RP170401 and RP160183), the MD Anderson Multidisciplinary Research Program, and philanthropic contributions to the Melanoma Moon Shots Program of MD Anderson. R.K. Jain and M.G. Vander Heiden were supported by a Dana-Farber Harvard Cancer Center/MIT Koch Institute Bridge Project grant. R.K. Jain is also supported by the Lustgarten Foundation; a grant from the Ludwig Center at Harvard; NCI grants P01 CA080124, R01 CA126642, R01 CA085140, R01 CA115767, R01 CA098706, R01 CA208205, U01 CA224173, and R35 CA197743; and U.S. Department of Defense Breast Cancer Research Program Innovator Award W81XWH-10-1-0016. M.G. Vander Heiden is also supported by the NIH (R21CA198028, R01CA168653), the MIT Ludwig Center, the MIT Center for Precision Cancer Medicine, a Stand Up To Cancer Innovative Research Grant, grant number SU2C-AACR-IRG-09-16, the Lustgarten Foundation, and a Faculty Scholar Grant from HHMI. Stand Up To Cancer (SU2C) is a division of the Entertainment Industry Foundation. The SU2C research grant is administered by the American Association for Cancer Research, the scientific partner of SU2C. E. Hernando is supported by the NIH/NCI R01CA2022027. NIH/NCI P01CA206980 (principal investigators: Berwick, Thomas), and NIH Melanoma SP0RE 1P50CA225450 (principal investigators: Osman, Weber). M. Mann is supported by the Max Planck Society for the Advancement of Science, the European Union's Horizon 2020 research and innovation program (Grant agreement no. 686547; MSmed project), the European Commission 7th Research Framework Program (GA ERC-202120Sylg\_318987; ToPAG project), and by the Novo Nordisk Foundation for the Clinical Proteomics group (grant NNF15CC0001). L.C. Cantley is supported by the NIH (NCI R35CA197588 and U54 CA210184), the Breast Cancer Research Foundation, the Gray Foundation Basser Initiative, and gifts from the Lori and Zachary Schreiber Family and the Roger and Susan Hertog Charitable Fund. M.E. Pacold is supported by a Mary Kay Foundation Cancer Research Grant (017-32), the Shifrin-Myers Breast Cancer Discovery Fund at NYULMC, a V Foundation V Scholar Grant funded by the Hearst Foundation (V2017-004), an NCI K22 Career Transition Award (1K22CA212059), a Career Enhancement Program Grant from the NYU Melanoma SP0RE (1P50CA225450; principal investigators: Osman, Weber), the Tara Miller Melanoma Foundation - MRA Young Investigator Award (MRA YIA 688365), and laboratory-directed research funding from the John and Elaine Kanas Family Foundation. The NYULMC CBRD, Metabolomics Core Resource Laboratory, and NYULMC Cores are partially funded by the NYUPCC Cancer Support Grant, NIH/NCI 5P30CA016087. The authors would like to thank all members of the Mann, Cantley, and Pacold Laboratories for critical feedback. We also thank Xin Li, Christopher Chin, and Miriam Sindelar for technical assistance, Tony T. Huang, Steven Gross, Lin Lin, Edouard Mullarky, and Costas Lysiotis for helpful discussions and technical advice, and the NYULH, WCMC, and MSK Small Animal Imaging Cores for assistance with MRI and BLI. Wild-type (Addgene plasmid 154917) and codon-optimized PHGDH were a gift of R. Possemato (Addgene plasmids 154915, 154916). We thank Huiyong Zhao (MSK Antitumor Assessment Core) and Arsen Mamakhanyan for technical assistance with Hyperpolarizer experiments. We thank Nelson Moss for preconsented brain metastasis specimens under approved IRB (177-067). We thank Iman Osman for the gift of the 12-273 short-term culture melanoma cell line. We are grateful for support from Luis Chiriboga and the NYU Center for Bio-specimen Research and Development and the NYU Metabolomics Core Resource Laboratory in acquiring and analyzing data.

The costs of publication of this article were defrayed in part by the payment of page charges. This article must therefore be hereby marked *advertisement* in accordance with 18 U.S.C. Section 1734 solely to indicate this fact.

Received October 22, 2019; revised April 15, 2020; accepted June 17, 2020; published first June 22, 2020.

## REFERENCES

- Bakhoum SF, Ngo B, Laughney AM, Cavallo J-A, Murphy CJ, Ly P, et al. Chromosomal instability drives metastasis through a cytosolic DNA response. *Nature* 2018;553:467–72.
- Smith HA, Kang Y. Determinants of organotropic metastasis. *Annu Rev Cancer Biol* 2017;1:403–23.
- McDonald OG, Li X, Saunders T, Tryggvadottir R, Mentch SJ, Warmoes MO, et al. Epigenomic reprogramming during pancreatic cancer progression links anabolic glucose metabolism to distant metastasis. *Nat Genet* 2017;49:367–76.
- Jacob LS, Vanharanta S, Obenaus AC, Pirun M, Viale A, Socci ND, et al. Metastatic competence can emerge with selection of preexisting oncogenic alleles without a need of new mutations. *Cancer Res* 2015;75:3713–9.
- Valiente M, Ahluwalia MS, Boire A, Brastianos PK, Goldberg SB, Lee EQ, et al. The evolving landscape of brain metastasis. *Trends Cancer* 2018;4:176–96.
- Kodack DP, Askoxylakis V, Ferraro GB, Fukumura D, Jain RK. Emerging strategies for treating brain metastases from breast cancer. *Cancer Cell* 2015;27:163–75.
- Achrol AS, Rennert RC, Anders C, Soffietti R, Ahluwalia MS, Nayak L, et al. Brain metastases. *Nat Rev Dis Primers* 2019;5:5.
- Ostrom QT, Wright CH, Barnholtz-Sloan JS. Brain metastases: epidemiology. *Handb Clin Neurol* 2018;149:27–42.
- Chen J, Lee H-J, Wu X, Huo L, Kim S-J, Xu L, et al. Gain of glucose-independent growth upon metastasis of breast cancer cells to the brain. *Cancer Res* 2015;75:554–65.
- Fischer GM, Jalali A, Kircher DA, Lee W-C, McQuade JL, Haydu LE, et al. Molecular profiling reveals unique immune and metabolic features of melanoma brain metastases. *Cancer Discov* 2019;9:628–45.
- Boire A, Zou Y, Shieh J, Macalino DG, Pentsova E, Massagué J. Complement component 3 adapts the cerebrospinal fluid for leptomeningeal metastasis. *Cell* 2017;168:1101–13.
- Varešlija D, Priedigkeit N, Fagan A, Purcell S, Cosgrove N, O'Halloran PJ, et al. Transcriptome characterization of matched primary breast and brain metastatic tumors to detect novel actionable targets. *J Natl Cancer Inst* 2019;111:388–98.
- Chen Q, Boire A, Jin X, Valiente M, Er EE, Lopez-Soto A, et al. Carcinoma-astrocyte gap junctions promote brain metastasis by cGAMP transfer. *Nature* 2016;533:493–8.
- Bos PD, Zhang XH-F, Nadal C, Shu W, Gomis RR, Nguyen DX, et al. Genes that mediate breast cancer metastasis to the brain. *Nature* 2009;459:1005–9.
- Priego N, Zhu L, Monteiro C, Mulders M, Wasilewski D, Bindeman W, et al. STAT3 labels a subpopulation of reactive astrocytes required for brain metastasis. *Nat Med* 2018;24:1024–35.
- Brastianos PK, Carter SL, Santagata S, Cahill DP, Taylor-Weiner A, Jones RT, et al. Genomic characterization of brain metastases reveals branched evolution and potential therapeutic targets. *Cancer Discov* 2015;5:1164–77.
- Er EE, Valiente M, Ganesh K, Zou Y, Agrawal S, Hu J, et al. Pericyte-like spreading by disseminated cancer cells activates YAP and MRTF for metastatic colonization. *Nat Cell Biol* 2018;20:966–78.
- Valiente M, Obenaus AC, Jin X, Chen Q, Zhang XH-F, Lee DJ, et al. Serpins promote cancer cell survival and vascular co-option in brain metastasis. *Cell* 2014;156:1002–16.
- Spector R, Robert Snodgrass S, Johanson CE. A balanced view of the cerebrospinal fluid composition and functions: focus on adult humans. *Exp Neurol* 2015;273:57–68.
- Dolgodilina E, Imobersteg S, Laczko E, Welt T, Verrey F, Makrides V. Brain interstitial fluid glutamine homeostasis is controlled by blood-brain barrier SLC7A5/LAT1 amino acid transporter. *J Cereb Blood Flow Metab* 2016;36:1929–41.
- Jones CM, Smith M, Henderson MJ. Reference data for cerebrospinal fluid and the utility of amino acid measurement for the diagnosis of inborn errors of metabolism. *Ann Clin Biochem* 2006;43:63–6.
- Rainesalo S, Keränen T, Palmio J, Peltola J, Oja SS, Saransaari P. Plasma and cerebrospinal fluid amino acids in epileptic patients. *Neurochem Res* 2004;29:319–24.
- Maggs DG, Jacob R, Rife F, Lange R, Leone P, During MJ, et al. Interstitial fluid concentrations of glycerol, glucose, and amino acids in human quadriceps muscle and adipose tissue. Evidence for significant lipolysis in skeletal muscle. *J Clin Invest* 1995;96:370–7.
- Muir A, Vander Heiden MG. The nutrient environment affects therapy. *Science* 2018;360:962–3.
- Davidson SM, Papagiannakopoulos T, Olenchock BA, Heyman JE, Keibler MA, Luengo A, et al. Environment impacts the metabolic dependencies of Ras-driven non-small cell lung cancer. *Cell Metab* 2016;23:517–28.
- Gui DY, Sullivan LB, Luengo A, Hosios AM, Bush LN, Gitego N, et al. Environment dictates dependence on mitochondrial complex I for NAD<sup>+</sup> and aspartate production and determines cancer cell sensitivity to metformin. *Cell Metab* 2016;24:716–27.
- Davidson SM, Jonas O, Keibler MA, Hou HW, Luengo A, Mayers JR, et al. Direct evidence for cancer-cell-autonomous extracellular protein catabolism in pancreatic tumors. *Nat Med* 2017;23:235–41.
- Sullivan MR, Vander Heiden MG. Determinants of nutrient limitation in cancer. *Crit Rev Biochem Mol Biol* 2019;282:1–15.
- Sullivan MR, Vander Heiden MG. When cancer needs what's non-essential. *Nat Cell Biol* 2017;19:418–20.
- Garcia-Bermudez J, Baudrier L, La K, Zhu XG, Fidelin J, Sviderskiy VO, et al. Aspartate is a limiting metabolite for cancer cell proliferation under hypoxia and in tumours. *Nat Cell Biol* 2018;20:775–81.
- Alkan HF, Walter KE, Luengo A, Madreiter-Sokolowski CT, Stryeck S, Lau AN, et al. Cytosolic aspartate availability determines cell survival when glutamine is limiting. *Cell Metab* 2018;28:706–6.
- Muir A, Danai LV, Gui DY, Waingarten CY, Lewis CA, Vander Heiden MG. Environmental cystine drives glutamine anaplerosis and sensitizes cancer cells to glutamine inhibition. *Elife* 2017;6:619.
- Sullivan MR, Mattaini KR, Dennstedt EA, Nguyen AA, Sivanand S, Reilly MF, et al. Increased serine synthesis provides an advantage for tumors arising in tissues where serine levels are limiting. *Cell Metab* 2019;29:1410–4.
- Sullivan MR, Danai LV, Lewis CA, Chan SH, Gui DY, Kunchok T, et al. Quantification of microenvironmental metabolites in murine cancers reveals determinants of tumor nutrient availability. *Elife* 2019;8:e44235.
- Cantor JR, Abu-Remaileh M, Kanarek N, Freinkman E, Gao X, Louissaint A, et al. Physiologic medium requires cellular metabolism and reveals uric acid as an endogenous inhibitor of UMP synthase. *Cell* 2017;169:258–72.
- Possemato R, Marks KM, Shaul YD, Pacold ME, Kim D, Birsoy K, et al. Functional genomics reveal that the serine synthesis pathway is essential in breast cancer. *Nature* 2011;476:346–50.
- Locasale JW, Grassian AR, Melman T, Lyssiotis CA, Mattaini KR, Bass AJ, et al. Phosphoglycerate dehydrogenase diverts glycolytic flux and contributes to oncogenesis. *Nat Genet* 2011;43:869–74.
- DeNicola GM, Karreth FA, Humpton TJ, Gopinathan A, Wei C, Frese K, et al. Oncogene-induced Nrf2 transcription promotes ROS detoxification and tumorigenesis. *Nature* 2011;475:106–9.
- Zhang B, Zheng A, Hydrbring P, Ambroise G, Ouchida AT, Goiny M, et al. PHGDH defines a metabolic subtype in lung adenocarcinomas with poor prognosis. *Cell Rep* 2017;19:2289–303.
- Pacold ME, Brimacombe KR, Chan SH, Rohde JM, Lewis CA, Swier LJYM, et al. A PHGDH inhibitor reveals coordination of serine synthesis and one-carbon unit fate. *Nat Chem Biol* 2016;12:452–8.
- Mullarky E, Lucki NC, Beheshti Zavareh R, Anglin JL, Gomes AP, Nicolay BN, et al. Identification of a small molecule inhibitor of 3-phosphoglycerate dehydrogenase to target serine biosynthesis in cancers. *Proc Natl Acad Sci U S A* 2016;113:1778–83.
- Reid MA, Allen AE, Liu S, Liberti MV, Liu P, Liu X, et al. Serine synthesis through PHGDH coordinates nucleotide levels by maintaining central carbon metabolism. *Nat Commun* 2018;9:5442.
- Chen J, Chung F, Yang G, Pu M, Gao H, Jiang W, et al. Phosphoglycerate dehydrogenase is dispensable for breast tumor maintenance and growth. *Oncotarget* 2013;4:2502–11.

44. Geiger T, Cox J, Mann M. Proteomic changes resulting from gene copy number variations in cancer cells. *PLoS Genet* 2010;6:e1001090.
45. Eckert MA, Coscia F, Chryplewicz A, Chang JW, Hernandez KM, Pan S, et al. Proteomics reveals NNMT as a master metabolic regulator of cancer-associated fibroblasts. *Nature* 2019;569:723–8.
46. Doll S, Gnad F, Mann M. The case for proteomics and phosphoproteomics in personalized cancer medicine. *Proteomics Clin Appl* 2019;13:e1800113.
47. Doll S, Kriegmair MC, Santos A, Wierer M, Coscia F, Neil HM, et al. Rapid proteomic analysis for solid tumors reveals LSD1 as a drug target in an end-stage cancer patient. *Mol Oncol* 2018;12:1296–307.
48. Coscia F, Lengyel E, Duraiswamy J, Ashcroft B, Bassani-Sternberg M, Wierer M, et al. Multi-level proteomics identifies CT45 as a chemosensitivity mediator and immunotherapy target in ovarian cancer. *Cell* 2018;175:159–70.
49. Mattaini KR, Sullivan MR, Vander Heiden MG. The importance of serine metabolism in cancer. *J Cell Biol* 2016;214:249–57.
50. Lin NU, Winer EP. Brain metastases: the HER2 paradigm. *Clin Cancer Res* 2007;13:1648–55.
51. Hofland KF, Thougard AV, Dejligbjerg M, Jensen LH, Kristjansen PEG, Rengtvad P, et al. Combining etoposide and dexrazoxane synergizes with radiotherapy and improves survival in mice with central nervous system tumors. *Clin Cancer Res* 2005;11:6722–9.
52. Rodriguez AE, Ducker GS, Billingham LK, Martinez CA, Mainolfi N, Suri V, et al. Serine metabolism supports macrophage IL-1 $\beta$  production. *Cell Metab* 2019;29:1003–4.
53. Aupérin A, Arriagada R, Pignon JP, Le Péchoux C, Gregor A, Stephens RJ, et al. Prophylactic cranial irradiation for patients with small-cell lung cancer in complete remission. Prophylactic Cranial Irradiation Overview Collaborative Group. *N Engl J Med* 1999;341:476–84.
54. Samanta D, Park Y, Andrabi SA, Shelton LM, Gilkes DM, Semenza GL. PHGDH expression is required for mitochondrial redox homeostasis, breast cancer stem cell maintenance, and lung metastasis. *Cancer Res* 2016;76:4430–42.
55. Schild T, Low V, Blenis J, Gomes AP. Unique metabolic adaptations dictate distal organ-specific metastatic colonization. *Cancer Cell* 2018;33:347–54.
56. Basnet H, Tian L, Ganesh K, Huang Y-H, Macalinao DG, Brogi E, et al. Flura-seq identifies organ-specific metabolic adaptations during early metastatic colonization. *Elife* 2019;8:5978.
57. Mashimo T, Pichumani K, Vemireddy V, Hatanpaa KJ, Singh DK, Sirasanagandla S, et al. Acetate is a bioenergetic substrate for human glioblastoma and brain metastases. *Cell* 2014;159:1603–14.
58. Scalise M, Pochini L, Panni S, Pingitore P, Hedfalk K, Indiveri C. Transport mechanism and regulatory properties of the human amino acid transporter ASCT2 (SLC1A5). *Amino Acids* 2014;46:2463–75.
59. Ni J, Ramkissoon SH, Xie S, Goel S, Stover DG, Guo H, et al. Combination inhibition of PI3K and mTORC1 yields durable remissions in mice bearing orthotopic patient-derived xenografts of HER2-positive breast cancer brain metastases. *Nat Med* 2016;22:723–6.
60. Shih DJH, Nayyar N, Bihun I, Dagogo-Jack I, Gill CM, Aquilanti E, et al. Genomic characterization of human brain metastases identifies drivers of metastatic lung adenocarcinoma. *Nat Genet* 2020;19:1511–7.
61. Reungwetwattana T, Nakagawa K, Cho BC, Cobo M, Cho EK, Bertolini A, et al. CNS response to osimertinib versus standard epidermal growth factor receptor tyrosine kinase inhibitors in patients with untreated EGFR-mutated advanced non-small-cell lung cancer. *J Clin Oncol* 2018;36:JCO2018783118–297.
62. Tawbi HA, Forsyth PA, Algazi A, Hamid O, Hodi FS, Moschos SJ, et al. Combined nivolumab and ipilimumab in melanoma metastatic to the brain. *N Engl J Med* 2018;379:722–30.
63. Murthy RK, Loi S, Okines A, Paplomata E, Hamilton E, Hurvitz SA, et al. Tucatinib, trastuzumab, and capecitabine for HER2-positive metastatic breast cancer. *N Engl J Med* 2020;382:597–609.
64. Vazquez A, Tedeschi PM, Bertino JR. Overexpression of the mitochondrial folate and glycine-serine pathway: a new determinant of methotrexate selectivity in tumors. *Cancer Res* 2013;73:478–82.
65. Vazquez A, Markert EK, Oltvai ZN. Serine biosynthesis with one carbon catabolism and the glycine cleavage system represents a novel pathway for ATP generation. *PLoS One* 2011;6:e25881.
66. Tedeschi PM, Markert EK, Gounder M, Lin H, Dvorzhinski D, Dolfi SC, et al. Contribution of serine, folate and glycine metabolism to the ATP, NADPH and purine requirements of cancer cells. *Cell Death Dis* 2013;4:e877–7.
67. Nikiforov MA, Chandriani S, O'Connell B, Petrenko O, Kotenko I, Beavis A, et al. A functional screen for Myc-responsive genes reveals serine hydroxymethyltransferase, a major source of the one-carbon unit for cell metabolism. *Mol Cell Biol* 2002;22:5793–800.
68. Sun L, Song L, Wan Q, Wu G, Li X, Wang Y, et al. cMyc-mediated activation of serine biosynthesis pathway is critical for cancer progression under nutrient deprivation conditions. *Cell Res* 2015;25:429–44.
69. Morrish F, Isern N, Sadilek M, Jeffrey M, Hockenbery DM. c-Myc activates multiple metabolic networks to generate substrates for cell-cycle entry. *Oncogene* 2009;28:2485–91.
70. Ducker GS, Ghergurovich JM, Mainolfi N, Suri V, Jeong SK, Hsin-Jung Li S, et al. Human SHMT inhibitors reveal defective glycine import as a targetable metabolic vulnerability of diffuse large B-cell lymphoma. *Proc Natl Acad Sci U S A* 2017;114:11404–9.
71. Dekhne AS, Ning C, Nayeem MJ, Shah K, Kalpage H, Frühauf J, et al. Cellular pharmacodynamics of a novel pyrrolo[3,2-d]pyrimidine inhibitor targeting mitochondrial and cytosolic one-carbon metabolism. *Mol Pharmacol* 2020;97:9–22.
72. Vandekerke S, Dubois C, Kalucka J, Sullivan MR, García-Caballero M, Goveia J, et al. Serine synthesis via PHGDH is essential for heme production in endothelial cells. *Cell Metab* 2018;28:573–87.
73. Kurniawan H, Franchina DG, Guerra L, Bonetti L, Baguet LS, Grusdat M, et al. Glutathione restricts serine metabolism to preserve regulatory T cell function. *Cell Metab* 2020;31:920–7.
74. Le Douce J, Maugard M, Veran J, Matos M, Jégo P, Vigneron P-A, et al. Impairment of glycolysis-derived l-serine production in astrocytes contributes to cognitive deficits in Alzheimer's disease. *Cell Metab* 2020;31:503–8.
75. Ma EH, Bantug G, Griss T, Condotta S, Johnson RM, Samborska B, et al. Serine is an essential metabolite for effector T cell expansion. *Cell Metab* 2017;25:345–57.
76. Kang YP, Falzone A, Liu M, Saller JJ, Karreth FA, DeNicola GM. PHGDH supports liver ceramide synthesis and sustains lipid homeostasis. *bioRxiv* 2019;1:861–43.
77. Kulak NA, Pichler G, Paron I, Nagaraj N, Mann M. Minimal, encapsulated proteomic-sample processing applied to copy-number estimation in eukaryotic cells. *Nat Methods* 2014;11:319–24.
78. Kelstrup CD, Jersie-Christensen RR, Barth TS, Arrey TN, Kuehn A, Kellmann M, et al. Rapid and deep proteomes by faster sequencing on a benchtop quadrupole ultra-high-field Orbitrap mass spectrometer. *J Proteome Res* 2014;13:6187–95.
79. Scheltema RA, Hauschild J-P, Lange O, Hornburg D, Denisov E, Damoc E, et al. The Q Exactive HF, a Benchtop mass spectrometer with a pre-filter, high-performance quadrupole and an ultra-high-field Orbitrap analyzer. *Mol Cell Proteomics* 2014;13:3698–708.
80. Cox J, Mann M. MaxQuant enables high peptide identification rates, individualized p.p.b.-range mass accuracies and proteome-wide protein quantification. *Nat Biotechnol* 2008;26:1367–72.
81. Cho K, Mahieu N, Ivanisevic J, Uritboonthai W, Chen Y-J, Siuzdak G, et al. isoMETLIN: a database for isotope-based metabolomics. *Anal Chem* 2014;86:9358–61.
82. Parker SJ, Svensson RU, Divakaruni AS, Lefebvre AE, Murphy AN, Shaw RJ, et al. LKB1 promotes metabolic flexibility in response to energy stress. *Metab Eng* 2017;43:208–17.
83. Wenig P, Odermatt J. OpenChrom: a cross-platform open source software for the mass spectrometric analysis of chromatographic data. *BMC Bioinformatics* 2010;11:405–9.
84. Fernandez CA, Rosiers Des C, Previs SF, David F, Brunengraber H. Correction of <sup>13</sup>C mass isotopomer distributions for natural stable isotope abundance. *J Mass Spectrom* 1996;31:255–62.

85. Lewis CA, Parker SJ, Fiske BP, McCloskey D, Gui DY, Green CR, et al. Tracing compartmentalized NADPH metabolism in the cytosol and mitochondria of mammalian cells. *Mol Cell* 2014;55:253–63.
86. Kodack DP, Chung E, Yamashita H, Incio J, Duyverman AMMJ, Song Y, et al. Combined targeting of HER2 and VEGFR2 for effective treatment of HER2-amplified breast cancer brain metastases. *Proc Natl Acad Sci U S A* 2012;109:E3119–27.
87. Yu M, Bardia A, Aceto N, Bersani F, Madden MW, Donaldson MC, et al. Cancer therapy. Ex vivo culture of circulating breast tumor cells for individualized testing of drug susceptibility. *Science* 2014;345:216–20.
88. Klotz R, Thomas A, Teng T, Han SM, Iriondo O, Li L, et al. Circulating tumor cells exhibit metastatic tropism and reveal brain metastasis drivers. *Cancer Discov* 2020;10:86–103.
89. Dong Y, Eskandari R, Ray C, Granlund KL, Santos-Cunha LD, Miloushev VZ, et al. Hyperpolarized MRI visualizes Warburg effects and predicts treatment response to mTOR inhibitors in patient-derived ccRCC xenograft models. *Cancer Res* 2019;79:242–50.
90. Harris T, Eliyahu G, Frydman L, Degani H. Kinetics of hyperpolarized  $^{13}\text{C}$ -pyruvate transport and metabolism in living human breast cancer cells. *Proc Natl Acad Sci U S A* 2009;106:18131–6.
91. Granlund KL, Tee SS, Vargas HA, Lyashchenko SK, Reznik E, Fine S, et al. Hyperpolarized MRI of human prostate cancer reveals increased lactate with tumor grade driven by monocarboxylate transporter 1. *Cell Metab* 2020;31:105–14.
92. Crane JC, Gordon JW, Chen H-Y, Autry AW, Li Y, Olson MP, et al. Hyperpolarized  $^{13}\text{C}$  MRI data acquisition and analysis in prostate and brain at University of California, San Francisco. *NMR Biomed* 2020;100:e4280.
93. Tee SS, DiGalleonardo V, Eskandari R, Jeong S, Granlund KL, Miloushev V, et al. Sampling hyperpolarized molecules utilizing a 1 Tesla permanent magnetic field. *Sci Rep* 2016;6:32846–6.